Available online at www.sciencedirect.com
ScienceDirect
Journal of Sound and Vibration 324 (2009) 365–386
JOURNAL OF SOUND AND VIBRATION
www.elsevier.com/locate/jsvi

Curve squealing of trains: Measurement, modelling and simulation

Ch. Glocker[a,*], E. Cataldi-Spinola[b], R.I. Leine[a]

[a]*IMES—Center of Mechanics, Department of Mechanical and Process Engineering, ETH Zurich, Zurich, Switzerland*
[b]*SBB Cargo, Officine Bellinzona, Bellinzona, Switzerland*

Received 9 September 2008; received in revised form 8 December 2008; accepted 26 January 2009
Handling Editor: M.P. Cartmell
Available online 20 March 2009

Abstract

Curve squealing of railway wheels occurs erratically in narrow curves with a frequency of about 4 kHz. Squealing is caused by a self-excited stick-slip oscillation in the wheel–rail contact. The mechanism which activates squeal is still unexplained and will be analyzed in the paper at hand. The squeal model consists of the first modal forms of an elastic wheel and is equipped with a three-dimensional hard Coulomb contact. Based on this model, a linear stability analysis of the stationary run through a curve is performed for the four wheels of the investigated bogie. The results show that in particular the front inner wheel tends to squeal. A numerical simulation of the system's differential inclusions performed on the unstable states shows the existence of a self-excited stick-slip oscillation. The computed frequency of the limit cycle agrees well with the measurements. The design of the squeal model, the steps necessary to perform the stability analysis on systems with non-ideal constraints, as well as the non-smooth dynamics code used to perform the simulations are explained in detail.

1. Introduction

Curve squealing occasionally arises when railway vehicles run through tight curves at low speed. It is characterized by a narrow-banded noise emission in the range of 4000 Hz, which normally occurs for some seconds. Despite of intensive and long-lasting research on this phenomenon, the mechanism behind squeal is still not fully understood, and the remedies against it lack in many cases on scientific confirmation. Curve squealing belongs to the class of self-induced vibrations. In contrast to external and parametric excitation, self-induced vibrations require the system to be nonlinear. The source of squeal has to be attributed to the wheel–rail contact: creep between wheel and rail, which always is present because of the kinematic design of the curved rails in combination with the wheel sets, induces frictional vibrations in the contacts which manifest themselves as structural oscillations of the wheels and rails. These vibrations are in the range of micrometers

*Corresponding author. Tel.: +41 44 632 5121; fax: +41 44 632 1145.
E-mail address: glocker@imes.mavt.ethz.ch (Ch. Glocker).

0022-460X/$ - see front matter © 2009 Elsevier Ltd. All rights reserved.
doi:10.1016/j.jsv.2009.01.048

because of the high frequencies at which squeal occurs, and are transferred as pressure oscillations to the embedding medium, i.e. the air, from which they are perceived as noise.

A cooperation has been started between the Swiss Federal Railways (SBB) in the person of Roland Müller and the Center of Mechanics at ETH Zurich. Within the framework of this cooperation, two doctoral theses [1,2] have recently been written. Together, they provide a rather complete analysis of curve squealing, from the mechanism of self-excitation up to the emission of noise, and may establish a basis for systematic development of counter measures. The work [2] has focused more on the experimental characterization of the squeal phenomenon, in which on-site measurement of the noise and the parameters responsible for it takes the center stage, together with the acoustic modelling and simulation of the noise emission of the wheel. In addition, a mechanical model of the mechanism of self-excitation has been developed in Ref. [1], for which the data from Ref. [2] have been used as inputs. The paper at hand reports on the results obtained for the numerical–experimental analysis of the mechanism of self-excitation. They are mainly taken from Ref. [1] but supplemented with certain measurements from Ref. [2] and a concise description of the theoretical setting on which the numerical codes are based.

Extensive experience in handling dry friction phenomena at the first author's institute have led to the strong belief that analyzing mechanisms of friction-induced vibrations requires utmost carefulness in both the modelling of the mechanical system and the selection of the numerical schemes. Because of these reasons, the following strategy has been chosen: In order to numerically analyze the squeal phenomenon, a mechanical model tailored for resolving frequencies up to 6 kHz has been developed. This model is presented in detail in Section 5. It consists of a single non-rotating elastic wheel with inertially fixed center and a rigid rail which moves with constant speed relative to the wheel according to the nominal creep that is present in curves. The interaction between the wheel and the rail is modelled by one frictional contact point, for which a hard unilateral constraint is used in the normal direction, and a Coulomb friction element with constant friction coefficient in the two tangential directions. The elastic modes of the wheel that are used in this squeal model have been extracted in a previous step from finite element (FE) computations with succeeding modal reduction of a real railway wheel. The FE model together with comparative measurements is presented in Section 3. In addition to the elastic modes of the wheel, the squeal model in Section 5 requires as inputs the location of the contact points, the inclination of the contact plane, the direction and magnitude of the nominal creep, and approximates of the nominal contact forces as they appear during a stable stationary run through a curve. In order to obtain these data, the stationary run of a specific driving trailer through a specific curve has been simulated with commercial multibody software and has been supplemented with measurements. In progress of the simulations, the system develops itself until a stationary state is reached and the nominal values of the required data at all wheels are available. The multibody model, consisting of the rail and the trailer with its two bogies, is presented in Section 4. For taking into account the wheel–rail interactions, the contact model of Polach has been used in the multibody simulation. This contact model has been proven to excellently meet the requirements of stationary or low-frequency dynamics as needed here to determine the nominal contact parameters, but it provides too less insight to structurally analyze the mechanism behind the high-frequency squeal dynamics. We have therefore intentionally used two different contact models for the computations, i.e. the Polach model for the low-frequency dynamics within the stationary run in Section 4, and the unilateral hard Coulomb contact for the high-frequency dynamics at the squeal phenomenon in Section 5 and beyond. Additional aspects on the special needs of the high-frequency contact dynamics model are addressed in Section 5. We furthermore want to stress that a combined numerical treatment of both the stationary run and the high-frequency squeal dynamics is not reasonable because of the different time-scales at which the associated dynamic phenomena occur: To achieve the stationary run, a track length of about 50 m is needed. This takes the train 12.5 s to go through when a driving speed of 4 m/s is assumed. On the other hand, the period at a squeal frequency of about 4 kHz is 250 μs, which makes a factor of 50 000 between the two time scales and forces the squeal model to be split from the model of the stationary run.

Based on the squeal model described in Section 5, curve squealing is numerically analyzed with the institute's research code in Sections 6 and 7. In Section 6, a linear stability analysis is performed on the stationary run through a curve. Due to the always existing creep, the system is exclusively in the slip state during this maneuver. Moreover, presence of Coulomb friction turns the persisting contact into a non-ideal constraint, which requires special steps to set up the linearized equations on which the stability of the system is

judged. It is shown in detail how linearization has to be performed for this particular case of a non-ideal constraint. In Section 7, results of the numerical simulation of curve squealing are presented, together with a full description of the integration scheme and the inequality solver used.

2. Measurements

In this section, some results of the field measurements performed in Ref. [2] are summarized. They will serve as a basis for developing the squeal model. Measurements have been taken during regular train service in three phases in a relatively tight curve (radius 200 m, gauge 1450 mm, cant 110 mm, rail inclination 1:40, rail type UIC54E) on track 303 near the station Bern-Ausserholligen, in which trains are running at low speed and squeal has been frequently reported to occur. The vehicles singled out for the measurements are particular regional trains of SBB (series 560) composed of a rail car, a driving trailer (type Bt 29–30) and some intermediate cars, which periodically run on this track. Only trains leaving the station Ausserholligen have been measured to not confuse the noise with break squeal.

Both sides of the track have been equipped with a free-field electret condenser microphone to record the noise generated by the squeal. The recorded signals have been processed by a moving window FFT and displayed as color-coded frequency–time diagrams, in which the time instants of the wheel axles passing the microphones have additionally been marked (Fig. 1, without indication of the axles). In order to measure the vibrations of the rails, triaxial acceleration sensors have been installed at the bottom of both rails. The velocity of the axles passing by has initially been determined by axle counters, but has later been replaced by a couple of laser distance sensors on each rail. In this way, the lateral displacements and the angles of attack of the wheels relative to the rail have been accessed from the distances measured to the wheel rims.

Fig. 1 shows the frequency spectrum of the noise of a train passing by, which has been recorded by one of the microphones. Squeal can be observed between 12 and 18 seconds. In addition to the fundamental frequency of about 4 kHz, distinct superharmonics at 8 and 12 kHz are clearly visible in the diagram, which points at the strong nonlinear character of squeal. Furthermore, one observes a slight shift of about 150 Hz in the fundamental frequency, which occurs at the very instant at which the squealing wheel passes the microphone. This shift has also been found in the signals of the acceleration sensors and can be ascribed to the Doppler effect [2], indicating that the noise is mainly emitted from the wheel but not from the rail. This conclusion is drawn from the physical behavior that the wheel of a passing train can be regarded as a moving point source, whereas the rail acts as a non-moving line source for the emitted sound. Because of this, only the wheel is modelled in Section 3 as an elastic body, whereas the rail is considered as rigid for the entire analysis. Flange noise can also be observed in Fig. 1. It occurs between 2 and 6 seconds and can clearly be distinguished from curve squealing, as it is characterized by a wide-band frequency spectrum caused by the front outer wheel of the associated bogie.

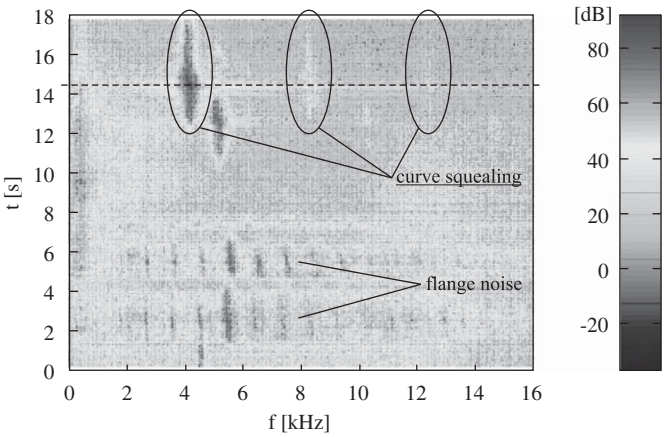

Fig. 1. Frequency spectrum of the noise recorded at one microphone for a train passing by. Recording has been initiated when the first wheel set passes the microphone.

The measurements reported in Ref. [2] mount up to 3085 train passages, of which 524 can be assigned to four particular trains, which have been singled out as noticeably noisy by their maximal sound intensity levels. Out of them, 83 passages have been judged as squealing by visual inspection of their frequency spectra and audio tests of the recorded noise. The wheels responsible for squealing have been identified by the axle counters and by comparing the noise intensity and acceleration levels of the measurements taken at the inside and outside of the curve. In 62 out of those 83 events, squealing has been uniquely attributed to the inside of the curve, which confirms the observations in Refs. [3,4]. Squealing at the outside has been observed occasionally, but much less frequently. In 32 out of the 62 squealing events at the inside of the curve, the squealing wheel has been found to be the leading inner wheel of the leading bogie of the driving trailer, and squealing has been around 4100 Hz. Because of this accumulation of squealing events, one has chosen the driving trailer to be the vehicle subjected to closer investigation (Section 4), and its utmost front inner wheel the one of central interest. Furthermore, measurements have revealed that squealing trains keep their ability to squeal robustly over weeks. This refers not only to the source of squeal within the train, but also to the squealing frequency that has been unaltered in such cases.

3. Elastic FE model of the wheel

For the FE analysis of the elastic wheel (elasticity modulus $2.068 \times 10^{11}\,\mathrm{N/m^2}$, Poisson ratio 0.29, density $7820\,\mathrm{kg/m^3}$) commercial software has been used. Fig. 2(b) shows a cross-section of the mesh which has been modelled by 8-node linear solid elements and which has been proven to be reliable up to frequencies of about 6000 Hz. The mesh is designed at the wheel rim in such a way that changes in the wheel diameter can easily be adjusted without remeshing. Such changes occur during the lifetime of a wheel due to reprofiling of the wheel surface as a maintenance procedure, which reduces the wheel diameter step by step from 820 mm for a new wheel to finally 760 mm for a worn wheel. The cross-section of the mesh in Fig. 2(b) consists of 122 elements, which results in a total of about 12 720 elements and 48 960 degrees of freedom for the wheel. Fig. 2(a) shows the position of the FE nodes on the tread of the wheel. This diagram is later used together with the wheel–rail profile pairing in Fig. 2(c) to determine the FE node on which the contact force acts. All calculations have been performed with a mesh that is fixed on the wheel. The rotation of the wheel relative to the mesh and the wandering of the contact force along the wheel's circumference during squeal, as well as centrifugal effects have been neglected. As reported in Ref. [5], those effects shift the natural frequencies of the wheel only by about 10 Hz because of the slow speeds at which squeal normally occurs.

The FE model of the wheel has been validated by measurements for two different situations, namely for a free wheel in the laboratory at ETH and for a wheel mounted on the driving trailer at the SBB works in Zurich. Measurements have been performed in form of an experimental modal analysis with a laser scanning vibrometer. The wheels have been excited on their rims in axial direction by a piezo element with a periodic

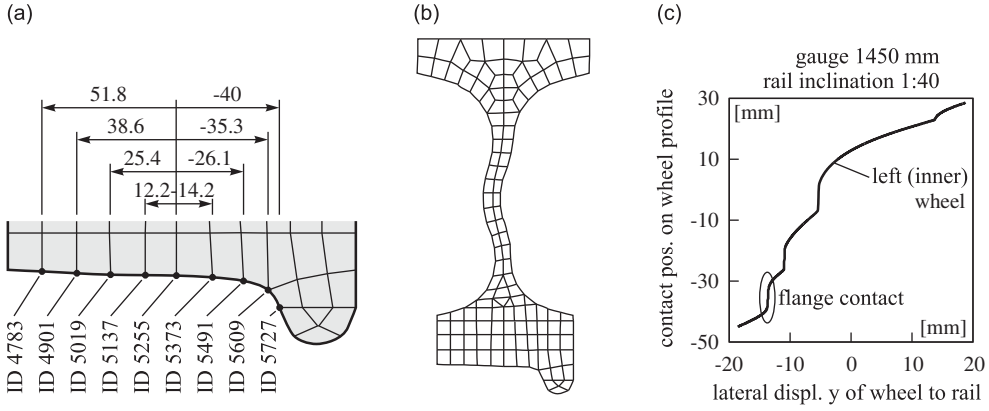

Fig. 2. The FE model of the wheel: (a) identification of the FE nodes on the tread for a wheel with 820 mm diameter, (b) cross-section of the mesh for a wheel with 820 mm diameter, and (c) wheel–rail profile pairing for wheel type S1002 and rail UIC54E.

chirp signal which went up to 10 kHz. Fig. 3 shows the results of this comparison for three selected eigenforms of a wheel with 820 mm diameter. In Fig. 3(a), computed eigenforms are shown for the two boundary conditions that the wheel is either freely floating or inertially fixed in three directions at its center nodes. The latter takes into account the connection to the axle as it is for a mounted wheel, of which the measurements are being displayed in Fig. 3(c). All measurements and calculations for the free wheel have also been conducted for a wheel diameter of 760 mm. For all cases investigated, the computed eigenfrequencies deviate less than 5% over the entire frequency spectrum of up to 6 kHz from those having been measured by the method described above. Interestingly, the wheel–rail contact, which naturally has been present in the measurements of the mounted wheel but which has not been considered in the FE calculations, seems to have only a minor influence on the results: If possible, the eigenforms align themselves at the wheel in such a way that one of their nodal points agrees with the wheel–rail contact point. In other words, the dynamics of the mounted wheel under contact with the rail seems to be adequately representable by the eigenforms computed for the wheel with only the center nodes fixed. This set of eigenforms will therefore be used as the shape functions for the squeal model to be developed in Section 5.

During the lifetime of a wheel, its diameter changes from 820 to 760 mm, which causes a reduction in mass from 258 to 190 kg. The wheel therefore looses nearly 70 kg of the material on its rim, which due to the reduced mass and stiffness results in a heavy shift of its eigenfrequencies. The effect of this shift on the squeal phenomenon will be discussed in Section 6. Fig. 4 shows a wheel with fixed center nodes, for which the eigenfrequencies have been computed for diameters of 820, 800, 780 and 760 mm. The resulting points in the diagram have been connected by straight lines for a better display of the arising frequency shifts. The lines are numbered consecutively in increasing order with respect to the eigenfrequencies that the wheel has at a diameter of 820 mm. Lines with double numbers refer to eigenforms which occur in pairs with a phase shift of 90° relative to each other, and which position themselves uniquely in angular direction at the rail as soon as the wheel–rail contact point has been taken into account. Some lines are drawn in heavy black. They refer to eigenforms which turned out to be important for squeal. The same line type has been used for eigenforms with similar modal shape. Solid lines in heavy black are assigned to eigenforms with only radial nodal lines but no nodal circles, for which the wheel rim exhibits heavy out-of-plane oscillations. Mode 35–36 (depicted) has 12 nodal lines, mode 50–51 has 14 nodal lines. Eigenforms addressed by dashed and dotted lines in heavy black have in common that they allow for a radial pulsation of the wheel rim. Modes 27–28, 31–32 (depicted), and 42–43 are represented by dashed lines. They are characterized by a triangular-, tetragonal- (depicted), and

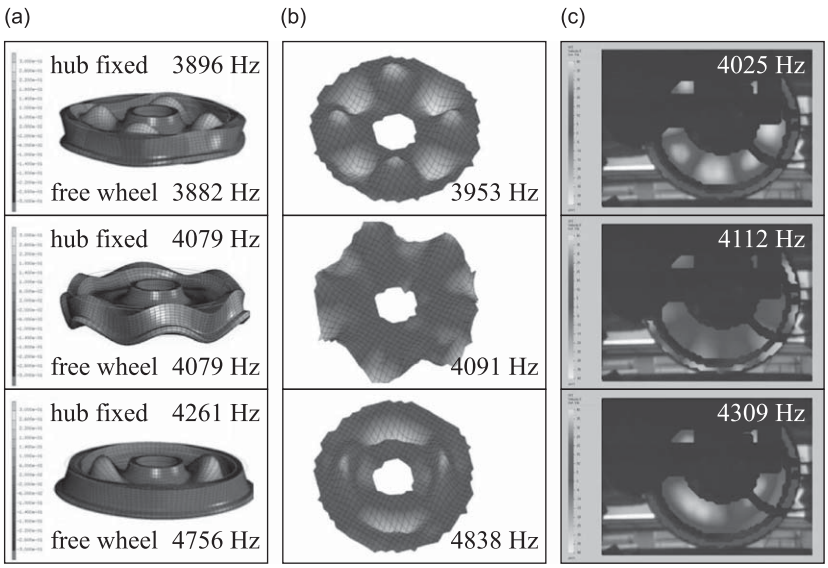

Fig. 3. Calculations versus measurements of selected eigenforms under different boundary conditions for a wheel with a diameter of 820 mm: (a) FE computations for a wheel with fixed and free center nodes, (b) measurements on a free wheel at ETH laboratory, and (c) measurements on a mounted wheel at SBB works.

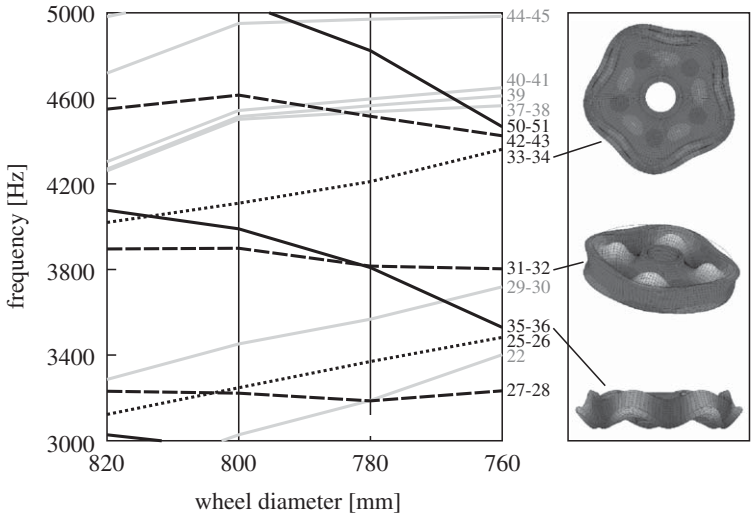

Fig. 4. Computed shift of the eigenfrequencies f_i of a wheel with fixed center nodes for various diameters.

Table 1
Computed eigenfrequencies f_i of the wheel with fixed hub (Fig. 3(a)) and measured modal damping values ζ_i of the mounted wheel (Fig. 3(c)) for a selection of modes and a wheel diameter of 820 mm.

Mode no.	25–26	27–28	31–32	33–34	35–36	42–43	50–51
Eigenfrequency f_i (Hz)	3125	3230	3896	4022	4079	4553	5161
Modal damping ζ_i (–)	0.0005	0.0036	0.00057	0.00065	0.00144	0.00055	0.0085

pentagonal-shaped radial vibration of the rim with heavy out-of-plane oscillations of the wheel disk, having 6, 8 (depicted), and 10 antinodal points circularly distributed on the disk. Modes 25–26 and 33–34 (depicted) are represented by dotted lines. They are characterized by a nearly pure in-plane vibration of the entire wheel, leading to tetragonal- and pentagonal-shaped (depicted) vibrations of the rim in mainly radial direction with slight out-of-plane components.

Along with the measurements on the mounted wheel in Fig. 3(c), the modal damping values ζ_i of all eigenforms up to 6 kHz have been determined. For eigenfrequencies which are well separated from each other, the associated modal damping values ζ_i have been obtained via their quality factors $Q_i = 1/(2\zeta_i)$ from the amplitude–frequency response curves. For eigenfrequencies close to each other, an analytical multi-mode model [1] has been used to approximate locally the measured amplitude–frequency response and to identify in this way the remaining ζ_i. Table 1 lists as representatives the eigenfrequencies f_i and modal damping values ζ_i of certain modes for a wheel with a diameter of 820 mm. The modes selected in the table are those that are marked with black lines in Fig. 4, i.e. those that we think to be important for squeal.

4. Multibody simulation of the stationary run

For the simulation of stationary runs through curves of the driving trailer, type Bt 29–30, a commercial multibody simulation program has been used. The model of the driving trailer is schematically depicted in Fig. 5. It consists of the car body, the two bogie frames and the four wheel sets, which are connected to the bogies by axle guides. All bodies are modelled as rigid. The catch, the primary suspensions, the secondary suspensions which contain an air spring model according to Krettek–Grajnert [6], the anti-roll bar, the vertical primary damper as well as the lateral dampers are represented as force elements. All data are as much as possible extracted from the technical documentation of the vehicle or have been chosen in close cooperation with railway vehicle experts. The track in Ausserholligen is composed of three sections in the model: The first

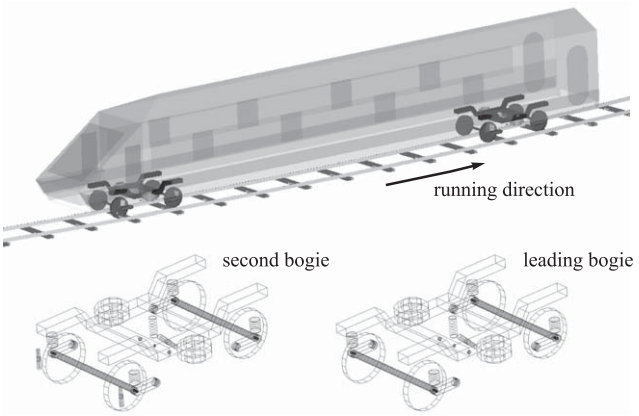

Fig. 5. Multibody model of the driving trailer and of its two bogies.

section is a 15 m long straight track. Then follows a 15 m long transition curve in which the cant of 110 mm and the curvature is uniformly established. Finally, the track ends with the curve of constant radius of 200 m. The complete track has been modelled with an inclination of 1:40, a gauge of 1450 mm and the standard rail profile UIC54E. Flexibility of the rail and supporting underground as well as all sorts of irregularities have not been considered. All calculations have been conducted with the standard wheel profile S1002 and the wheel–rail contact model of Polach [7] which has been available in the multibody code. A detailed description of the multibody model together with a list of all parameter values can be found in Ref. [1].

Fig. 6 depicts the coordinates which are necessary for the interpretation of the simulation results. They are shown exemplary for the left wheels, i.e. the curve-inner wheels of each wheel set. For each wheel, a reference system $(\mathbf{e}_x^R, \mathbf{e}_y^R, \mathbf{e}_z^R)$ is defined, of which the $\mathbf{e}_x^R$-axis lies in the horizontal plane and is tangential to the rail in the contact point. The $\mathbf{e}_y^R$-axis is inclined with respect to the horizontal plane by the cant angle. In addition, a contact system $(-\mathbf{n}, \mathbf{t}_1, \mathbf{t}_2)$ is introduced for each wheel, of which the orientation is determined by the simulation results and therefore not a priori known. This contact system follows from the angle of attack β around the $\mathbf{e}_z^R$-axis, and, subsequently, from the contact angle α around the new $\mathbf{e}_x^R$-axis obtained from the original one by rotation about β. Herein, the vectors $\mathbf{t}_1$ and $\mathbf{t}_2$ span the contact plane, $\mathbf{n}$ is the contact normal, and $\mathbf{t}_1$ lies in the plane of the wheel. Except for the contact angle α, all angles are assumed to be small. It therefore does not play a role in which order the various angles are applied to finally arrive at the contact angle. Furthermore, it does not matter in which approximate radial directions the likewise small lateral displacements y of the wheel sets are interpreted.

The aim of the simulations is to predict the stationary motion of the driving trailer on the curved track for a chosen constant driving velocity and chosen friction coefficients. The nominal values of the resulting loads and contact-kinematical parameters of each wheel have to be extracted from these simulation results. Table 2 shows the illustrative results for the leading curve-inner wheel of the leading bogie, which have been calculated for a driving velocity of 4.1 m/s, being typical for curve squealing, and for various friction coefficients. The triple (f_x, f_y, f_z) denotes the components of the contact force acting on the wheel displayed in the reference system $(\mathbf{e}_x^R, \mathbf{e}_y^R, \mathbf{e}_z^R)$, (χ_{T1}, χ_{T2}) are the creep velocities of the wheel relative to the rail in the directions $(\mathbf{t}_1, \mathbf{t}_2)$ at the contact point, α and β are the resulting angle of attack and the contact angle, and y is the lateral displacement of the wheel set as defined in Fig. 6. From the lateral displacement y, the position of the contact point on the tread of the wheel can be determined by the wheel–rail profile pairing diagram in Fig. 2(c). Subsequently, the FE node closest to the contact point is identified from Fig. 2(a) which approximately determines the point at which the contact force acts. An interpolation between the FE nodes has not been conducted, because the squeal mechanism reacts much more sensitive to deviations in the direction of the contact force, which is determined by the creep direction and the angles α and β, than to deviations in the position of the contact point. In addition, the angle of attack β_m and the lateral displacement y_m have been measured by using a pair of laser distance sensors being attached to the rails on each side of the track, where various friction coefficients have been realized by artificial wetting of the rail surface. The entities β and y are

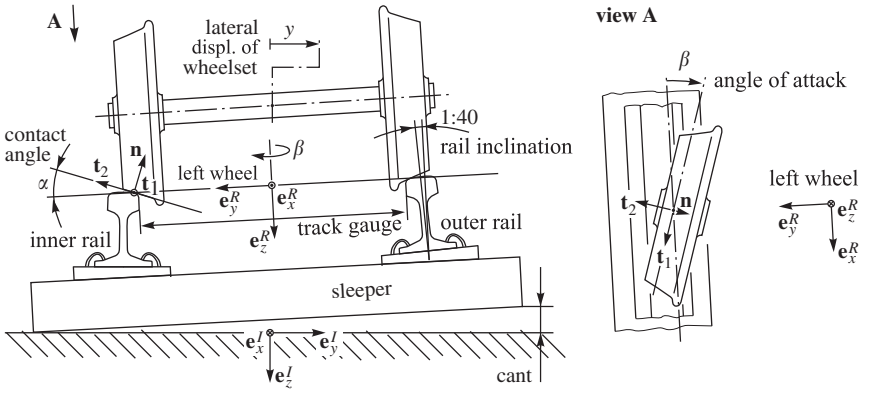

Fig. 6. Kinematic model of the wheel sets and definition of the associated coordinates.

Table 2
Results from the multibody simulation and measurements for the front inner wheel of the leading bogie at a driving velocity of 4.1 m/s.

μ (–)	f_x (kN)	f_y (kN)	f_z (kN)	χ_{T1} (mm/s)	χ_{T2} (mm/s)	α (deg)	β (mrad)	β_m (mrad)	y (mm)	y_m (mm)	Node ID
0.1	−0.04	−6.02	−50.62	0.4	−64.9	1.17	15.77	Wet	11.60	Wet	5019
0.2	−1.41	−11.02	−50.12	8.1	−61.3	1.38	14.92		13.49		5019
0.3	−3.61	−15.63	−49.90	13.4	−58.3	1.40	14.19	∼15	13.62	∼10.5	5019
0.4	−6.30	−20.01	−49.76	17.6	−57.0	1.40	13.87		13.64		5019
0.5	−9.28	−24.25	−49.74	20.4	−55.8	1.40	13.59		13.66		5019
0.6	−11.76	−28.70	−49.77	21.6	−54.9	1.41	13.38	Dry	13.67	Dry	5019

nearly constant for the leading wheel set of the bogie because of the already existing flange contact at the associated outer wheel. For the secondary wheel set, however, they depend strongly on the friction coefficient as follows from calculations [1] and measurements [2].

5. Design of the squeal model

Sections 3 and 4 provide all the data that are necessary to set up the squeal model illustrated in Fig. 7. In the model it is assumed that the center nodes of the wheel are fixed to the wheel reference frame $(\mathbf{e}_x^R, \mathbf{e}_y^R, \mathbf{e}_z^R)$ which acts as an inertial frame, whereas the rail is moving relative to the center of the wheel with the (now negative) creep velocities (χ_{T1}, χ_{T2}) in $(\mathbf{t}_1, \mathbf{t}_2)$-directions determined in Section 4. The actual creep velocities in the contact are therefore the superposition of the creep velocities (χ_{T1}, χ_{T2}) obtained for stationary motion and those stemming from elastic vibrations. The contact point at the wheel is denoted by C, the associated point on the rail by B.

The elastic model of the wheel uses the (symmetric and positive definite) mass and stiffness matrices $\mathfrak{M} \in \mathbb{R}^{n,n}$ and $\mathfrak{K} \in \mathbb{R}^{n,n}$ from the FE calculation for a wheel with fixed center nodes and n degrees of freedom. The Newton–Euler equation for the wheel can therefore be written as

$$\mathfrak{M}\ddot{\mathfrak{z}} + \mathfrak{K}\mathfrak{z} = \mathfrak{f}_C, \tag{1}$$

where $\mathfrak{z} \in \mathbb{R}^n$ denotes the displacements of the $n/3$ nodes that are located in the reference configuration at the positions $\mathfrak{p} \in \mathbb{R}^n$. The contribution $\mathfrak{f}_C$ of the contact force is still unknown and will be determined now from its virtual work δW_C and the displacement diagram Fig. 7(b). The node C on which the contact force $\mathbf{F}_C \in \mathbb{R}^3$ acts has already been determined in Section 4 and can be accessed by the (constant) node selection matrix $\mathbf{S}_C \in \mathbb{R}^{3,n}$. The positions $\mathbf{r}_{O\hat{C}} \in \mathbb{R}^3$ and $\mathbf{r}_{OC} \in \mathbb{R}^3$ of node C in the reference and the deformed configuration, its velocity $\mathbf{v}_C = \dot{\mathbf{r}}_{OC} \equiv \dot{\mathbf{r}}_{\hat{C}C} \in \mathbb{R}^3$ as the time derivative of the position difference $\mathbf{r}_{\hat{C}C}$ between $\hat{C}$ and C, and its

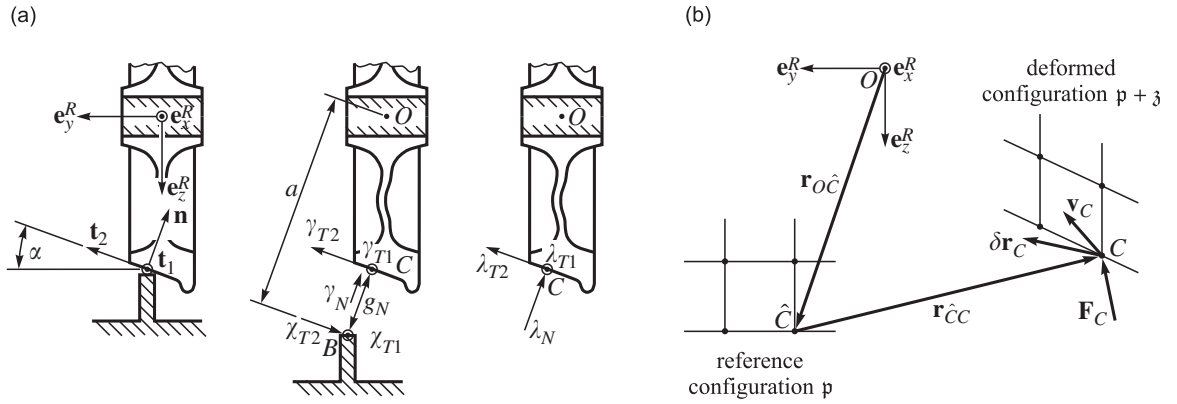

Fig. 7. The squeal model, consisting of the elastic wheel and the rigid rail: (a) from left to right: orientation of the inertial and the contact frame; definition of the contact kinematical entities; point of action and directions of the contact forces, and (b) application of the contact force $\mathbf{F}_C$ on the contact node C of the deformed wheel.

virtual displacement $\delta\mathbf{r}_C \in \mathbb{R}^3$ are therefore expressed as

$$\mathbf{r}_{O\hat{C}} = \mathbf{S}_C\mathfrak{p}, \quad \mathbf{r}_{OC} = \mathbf{S}_C(\mathfrak{p}+\mathfrak{z}), \quad \mathbf{v}_C = \mathbf{S}_C\dot{\mathfrak{z}}, \quad \delta\mathbf{r}_C = \mathbf{S}_C\delta\mathfrak{z}. \tag{2}$$

By invariance of the virtual work under coordinate transformations and the last equation in Eq. (2), one obtains from the virtual work of $\mathbf{F}_C$ the term

$$\delta W_C = \mathbf{F}_C^{\mathrm{T}}\delta\mathbf{r}_C = \mathbf{F}_C^{\mathrm{T}}\mathbf{S}_C\delta\mathfrak{z} =: \mathfrak{f}_C^{\mathrm{T}}\delta\mathfrak{z}, \tag{3}$$

from which the contribution $\mathfrak{f}_C$ of the contact force in Eq. (1) is identified as

$$\mathfrak{f}_C = \mathbf{S}_C^{\mathrm{T}}\mathbf{F}_C. \tag{4}$$

As displayed in the left and right diagram of Fig. 7(a), we finally decompose the contact force $\mathbf{F}_C$ into its components $(\lambda_N, \lambda_{T1}, \lambda_{T2})$ associated with the contact frame, of which the orientation has also been determined in Section 4,

$$\mathbf{F}_C = \mathbf{n}\lambda_N + \mathbf{t}_1\lambda_{T1} + \mathbf{t}_2\lambda_{T2}. \tag{5}$$

In this form, the scalar values λ_N and $(\lambda_{T1}, \lambda_{T2})$ of the normal force and the two tangential forces are later used to set up the contact laws.

The middle diagram in Fig. 7(a) shows the entities necessary to describe the kinematics of the contact. These are the contact gap g_N in normal direction which can directly be calculated from the nodal displacements (2) of point C,

$$g_N = \mathbf{n}^{\mathrm{T}}\mathbf{r}_{BC} = \mathbf{n}^{\mathrm{T}}(\mathbf{r}_{OC} - \mathbf{r}_{OB}) = \mathbf{n}^{\mathrm{T}}\mathbf{S}_C(\mathfrak{p}+\mathfrak{z}) + a = \mathbf{n}^{\mathrm{T}}\mathbf{S}_C\mathfrak{z} + \hat{a} \quad \text{with } \hat{a} := \mathbf{n}^{\mathrm{T}}\mathbf{S}_C\mathfrak{p} + a \text{ and } a := -\mathbf{n}^{\mathrm{T}}\mathbf{r}_{OB}, \tag{6}$$

and the relative velocities $(\gamma_N, \gamma_{T1}, \gamma_{T2})$ of point C with respect to point B on the rail. The normal relative velocity $\gamma_N = \dot{g}_N$ is obtained directly by projecting the nodal velocities (2) on the normal $\mathbf{n}$, whereas the tangential velocities γ_{Ti} consist of the differences in nodal velocities in the tangential directions and the creep velocities χ_{Ti},

$$\gamma_N = \mathbf{n}^{\mathrm{T}}(\mathbf{v}_C - \mathbf{v}_B) = \mathbf{n}^{\mathrm{T}}\mathbf{S}_C\dot{\mathfrak{z}}, \quad \gamma_{T1} = \mathbf{t}_1^{\mathrm{T}}(\mathbf{v}_C - \mathbf{v}_B) = \mathbf{t}_1^{\mathrm{T}}\mathbf{S}_C\dot{\mathfrak{z}} + \chi_{T1}, \quad \gamma_{T2} = \mathbf{t}_2^{\mathrm{T}}(\mathbf{v}_C - \mathbf{v}_B) = \mathbf{t}_2^{\mathrm{T}}\mathbf{S}_C\dot{\mathfrak{z}} + \chi_{T2}. \tag{7}$$

The two creep velocities χ_{Ti} obtained for stationary motion through the curve therefore enter the model as kinematic excitation.

The wheel–rail contact is modelled as a hard unilateral constraint with spatial Coulomb friction and constant friction coefficient μ. The contact law in normal direction displayed on velocity level [8] reads as

$$g_N > 0 \Rightarrow -\lambda_N = 0, \quad g_N = 0: \quad \begin{cases} \gamma_N > 0 & \Rightarrow -\lambda_N = 0 \\ \gamma_N = 0 & \Rightarrow -\lambda_N \leqslant 0 \end{cases} \tag{8}$$

and contains the states of enduring and open contact, as well as the lift-off transition. The transition from an open to a closed contact is not yet taken into account in Eq. (8), because it would require in addition an impact law as it is later introduced in Section 7. The conditions from left to right in Eq. (8) have the following physical meaning: For an open contact $g_N > 0$ the normal contact force vanishes, $\lambda_N = 0$. For a closed contact $g_N = 0$, the further evolution depends on the normal relative velocities $\gamma_N = \dot{g}_N$: For $\gamma_N > 0$, the contact will immediately open in near future, thus the (right limit of the) contact force has to disappear, $\lambda_N = 0$. For $\gamma_N = 0$, the contact may stay closed with λ_N acting as a compressive force, $\lambda_N \geqslant 0$. Although the state of an open contact, and the lift-off and touch-down transition as a consequence, are most unexpectedly to occur for curve squealing, they have been kept in the formulation because of two reasons: First, for an oscillation of 4 kHz they cannot be pre-excluded with final guarantee. Secondly, there is nearly no extra effort to keep them in the algorithm [9] presented in Section 7. In tangential directions, the Coulomb friction law is employed which reads as

$$\begin{cases} \boldsymbol{\gamma}_T \neq 0 & \Rightarrow -\boldsymbol{\lambda}_T = \mu\lambda_N \mathbf{e}_T(\boldsymbol{\gamma}_T) \\ \boldsymbol{\gamma}_T = 0 & \Rightarrow \| -\boldsymbol{\lambda}_T \| \leqslant \mu\lambda_N \end{cases} \quad \text{with} \quad \mathbf{e}_T(\boldsymbol{\gamma}_T) = \frac{\boldsymbol{\gamma}_T}{\|\boldsymbol{\gamma}_T\|} \tag{9}$$

and $\boldsymbol{\lambda}_T = (\lambda_{T1}\ \lambda_{T2})^{\mathrm{T}}$, $\boldsymbol{\gamma}_T = (\gamma_{T1}\ \gamma_{T2})^{\mathrm{T}}$, $\boldsymbol{\chi}_T = (\chi_{T1}\ \chi_{T2})^{\mathrm{T}}$. The friction law makes a clear distinction between stiction and sliding: If the contact is sliding $\boldsymbol{\gamma}_T \neq 0$, then the friction force $\boldsymbol{\lambda}_T$ has the magnitude $\mu\lambda_N$ and opposes the sliding direction $\mathbf{e}_T$. For a vanishing tangential relative velocity $\boldsymbol{\gamma}_T = 0$, the contact may be in stiction, thus we have to allow tangential contact forces $\boldsymbol{\lambda}_T$ with a magnitude even smaller than $\mu\lambda_N$. Drilling friction (pivoting friction) is not considered, as it is not essential for the squeal mechanism.

The dependency of the friction coefficient on the relative velocity, which is generally known as the Stribeck effect, has deliberately been omitted in the modelling. If one imagines the conditions under which curve squealing occurs in praxis, then it is implausible that the menagerie of decreasing friction curves that are used in the literature [10–13] are responsible for this phenomenon: We have to keep in mind that squeal typically occurs with a frequency of about 4 kHz and lasts in the case of Fig. 1 for about five seconds. At a velocity of 4 m/s, this corresponds with a distance of 20 m over the track on which the wheel undergoes 20 000 periods of oscillation. This implies that the wheel travels the distance of 1 mm per oscillation period, which is very large with respect to a typical amplitude of oscillation of 5 μm. Each period of oscillation therefore occurs at a completely different location on the track, i.e. 20 000 different locations on 20 m. If one takes a closer look on a real railway track which is subjected to everyday's environmental conditions and wear processes (abrasion, corrosion, dirt, surface irregularities, etc.), then it is doubtful that the frictional conditions on all these 20 000 locations have to be described by just one particular friction curve. Moreover, it is questionable whether the classical understanding of stiction and slipping still makes sense for displacements of 5 μm being of the same order of magnitude as the size of small asperities and big metal grains. We therefore believe that squeal is a rather stable oscillation mechanism which is very insensitive to the exact form of the chosen friction curve and should therefore be reproducible even by the simplest one. For this reason, we propose in this paper an oscillation mechanism for squeal which is insensitive to the slope of the friction curve, either being negative or even slightly positive, and has therefore been chosen to be constant for the numerical calculation. The reason why almost always a decreasing friction curve is adopted in literature lies in the insufficient modelling of the dynamics of the wheel. Typically, the dynamics of the physical system is reduced to a mechanical one-degree-of-freedom system having the structure of the classical block-on-belt model [14,15], which can only exhibit a self-excited periodic oscillation if a decreasing friction curve is chosen. In Ref. [16] it is therefore suggested to extend the common lateral models for squeal with forces in longitudinal and normal direction which only makes sense if the wheel can dynamically respond in these directions. From the literature [17–19] it is known that systems with degrees of freedom in normal and tangential direction of the contact can exhibit friction-induced self-excited oscillations, even if the falling slope of the friction curve is not present. These self-excited oscillations are caused by the proportionality between the friction force and the normal force during sliding, as well as the coupling between the normal and tangential degrees of freedom. The mechanical model proposed in the paper at hand contains degrees of freedom in normal and tangential directions by the elastic model of the wheel and can therefore exhibit the aforementioned friction-induced self-excited oscillations. Consequently, our model gives a mechanism for squeal which is, in a certain range, insensitive on the chosen friction curve.

The squeal model, being completely determined by Eqs. (1) and (4)–(9) in nodal displacements $\mathfrak{z} \in \mathbb{R}^n$, is subsequently reduced to the first $f = 61$ eigenforms $\mathfrak{u}_i \in \mathbb{R}^n$ from Section 3. They sufficiently approximate the system up to 6 kHz. With $\mathfrak{U} := (\mathfrak{u}_1, \ldots, \mathfrak{u}_f) \in \mathbb{R}^{n,f}$ and $\mathbf{q} \in \mathbb{R}^f$ the associated modal amplitudes, one sets by the classical reduction technique $\mathfrak{z} = \mathfrak{U}\mathbf{q}$ to obtain via differentiation and variation the kinematical transformations

$$\mathfrak{z} = \mathfrak{U}\mathbf{q}, \quad \dot{\mathfrak{z}} = \mathfrak{U}\dot{\mathbf{q}}, \quad \ddot{\mathfrak{z}} = \mathfrak{U}\ddot{\mathbf{q}}, \quad \delta\mathfrak{z} = \mathfrak{U}\delta\mathbf{q}. \tag{10}$$

Reduction of Eq. (1) is now classically performed with the help of the associated virtual work expression and the kinematic transformations (10), which yields

$$0 = \delta W = \delta\mathfrak{z}^{\mathrm{T}}(\mathfrak{M}\ddot{\mathfrak{z}} + \mathfrak{K}\mathfrak{z} - \mathfrak{f}_C) = \delta\mathbf{q}^{\mathrm{T}}\mathfrak{U}^{\mathrm{T}}(\mathfrak{M}\mathfrak{U}\ddot{\mathbf{q}} + \mathfrak{K}\mathfrak{U}\mathbf{q} - \mathfrak{f}_C) \quad \forall\delta\mathbf{q}. \tag{11}$$

After elimination of $\mathfrak{f}_C$ in Eq. (11) by Eqs. (4) and (5), and by taking the eigenforms $\mathfrak{u}_i$ such that they are already normalized with respect to the system's mass matrix $\mathfrak{M}$, we set

$$\mathbf{M} := \mathfrak{U}^{\mathrm{T}}\mathfrak{M}\mathfrak{U} = \mathbb{1}, \quad \mathbf{K} := \mathfrak{U}^{\mathrm{T}}\mathfrak{K}\mathfrak{U} = \mathrm{diag}(\omega_i), \quad \mathbf{w}_N := \mathfrak{U}^{\mathrm{T}}\mathbf{S}_C^{\mathrm{T}}\mathbf{n}, \quad \mathbf{W}_T := \mathfrak{U}^{\mathrm{T}}\mathbf{S}_C^{\mathrm{T}}(\mathbf{t}_1, \mathbf{t}_2) \tag{12}$$

to arrive at the Newton–Euler equations for the reduced system in the form

$$\mathbf{M}\ddot{\mathbf{q}} + \mathbf{D}\dot{\mathbf{q}} + \mathbf{K}\mathbf{q} - \mathbf{w}_N\lambda_N - \mathbf{W}_T\boldsymbol{\lambda}_T = 0. \tag{13}$$

The Newton–Euler equations expressed in the $f = 61$ modal amplitudes $\mathbf{q}$ are therefore composed of the identity mass matrix $\mathbf{M} \in \mathbb{R}^{f,f}$, the constant and positive definite diagonal stiffness matrix $\mathbf{K} \in \mathbb{R}^{f,f}$ with the eigenfrequencies ω_i as its entries, and the three constant generalized force directions $\mathbf{w}_N \in \mathbb{R}^f$, $\mathbf{W}_T \in \mathbb{R}^{f,2}$ for the three contact forces $\lambda_N, \boldsymbol{\lambda}_T$. In addition, the modal damping values ζ_i of these 61 eigenforms are taken into account in Eq. (13) by the diagonal and positive definite damping matrix $\mathbf{D} = \mathrm{diag}(2\omega_i\zeta_i) \in \mathbb{R}^{f,f}$ with $\omega_i = 2\pi f_i$ and f_i the associated eigenfrequencies as displayed for a selection of modes in Table 1.

The kinematical relationships (6) and (7) have also to be transformed to the new variables $\mathbf{q}$, which is again performed with the help of Eq. (10). The resulting terms for the contact gap and the relative velocities are

$$g_N = \mathbf{w}_N^{\mathrm{T}}\mathbf{q} + \hat{a}, \quad \gamma_N = \mathbf{w}_N^{\mathrm{T}}\dot{\mathbf{q}}, \quad \boldsymbol{\gamma}_T = \mathbf{W}_T^{\mathrm{T}}\dot{\mathbf{q}} + \boldsymbol{\chi}_T \tag{14}$$

for which the same expressions $\mathbf{w}_N$, $\mathbf{W}_T$ occur as in Eq. (12). The gap function g_N depends now in principle on all the 61 modal amplitudes $\mathbf{q}$ which serve as the generalized coordinates. Similarly, the relative velocities $\gamma_N, \boldsymbol{\gamma}_T$ are dependent on the 61 modal velocities $\dot{\mathbf{q}}$. In a last step, the distance a (Fig. 7(a)) between the wheel center and the rail is adjusted such that the resulting normal contact force λ_N in the reduced (temporarily frictionless) model agrees with the associated component of the contact forces (f_x, f_y, f_z) obtained from the multibody simulation, i.e. $\lambda_N = \mathbf{n}^{\mathrm{T}}(f_x, f_y, f_z)$. Note that a is not a constant geometric value but accounts for the deformation of the deformable wheel under load. Due to the boundary conditions that we have chosen for the model (rail inertially fixed, center of wheel inertially fixed), it is needed to pre-load the wheel according to its nominal state.

The reduced system is now completely described by the Newton–Euler equations (13), contact kinematics (14), and the contact laws (8) and (9). Together, they constitute the equations of motion for our squeal model, and all succeeding investigations are based on them. Unknowns are the evolution of $\mathbf{q}(t)$, $g_N(t)$, $(\gamma_N, \boldsymbol{\gamma}_T)(t)$ and $(\lambda_N, \boldsymbol{\lambda}_T)(t)$.

6. Stability analysis of the stationary run

In this section, the stability of the stationary run through a curve is analyzed, driven by the following concept: The equations of motion (13), (14), (8) and (9) are general in the sense that they contain all the different possible states of the system, i.e. enduring open contact, enduring closed contact with stiction, enduring closed contact with sliding, and all the transitions between them (except for the impacts). The stationary run through the curve is characterized by a solution $\mathbf{q}_0(t)$ of the equations of motion, for which the wheel does not vibrate, i.e. for which $\mathbf{q}_0 = \text{const.}$ and $\dot{\mathbf{q}}_0 = \ddot{\mathbf{q}}_0 = 0$ as a consequence. It can be shown that a solution of the particular form $\mathbf{q}_0 = \text{const.}$, which is called an equilibrium point of the system, fulfills in our case the equations of motion for one and only one state, which is enduring closed contact with sliding. As long

as the equilibrium is not at the boundary of this state, small superimposed oscillations will not cause the system to leave this state, and first-order stability of the equilibrium can be investigated classically, i.e. by linearization of the equations of motion in this state at the equilibrium point. This approach follows the theory in Ref. [20], in which general theorems on the stability of motion of systems with hard Coulomb contact are presented.

In order to proceed, we first have to extract the state of enduring contact with slip from the equations of motion (13), (14), (8) and (9). Sliding ($\gamma_T \neq 0$) means that the first equation in the tangential contact law (9) holds true, which enables us to express the tangential force $\boldsymbol{\lambda}_T$ in Eq. (13) in terms of its normal force,

$$\mathbf{M}\ddot{\mathbf{q}} + \mathbf{D}\dot{\mathbf{q}} + \mathbf{K}\mathbf{q} - (\mathbf{w}_N - \mu \mathbf{W}_T \mathbf{e}_T(\dot{\mathbf{q}}))\lambda_N = 0 \quad \text{with } \mathbf{e}_T(\dot{\mathbf{q}}) = \frac{\mathbf{W}_T^{\mathrm{T}}\dot{\mathbf{q}} + \boldsymbol{\chi}_T}{\|\mathbf{W}_T^{\mathrm{T}}\dot{\mathbf{q}} + \boldsymbol{\chi}_T\|}. \tag{15}$$

Enduring contact means that the gap function $g_N(t)$ is equal to zero within some open time interval, $g_N(t) = 0$ for $t \in (t_1, t_2)$, and so its time derivatives $\gamma_N(t) = \dot{\gamma}_N(t) = 0$ which follows from differentiation. For enduring contact, the normal contact law (8) is therefore reduced to an equality law $g_N = 0$, $\gamma_N = 0$, $\dot{\gamma}_N = 0$, which yields with Eq. (14)

$$g_N = \mathbf{w}_N^{\mathrm{T}}\mathbf{q} + \hat{a} = 0, \quad \gamma_N = \mathbf{w}_N^{\mathrm{T}}\dot{\mathbf{q}} = 0, \quad \dot{\gamma}_N = \mathbf{w}_N^{\mathrm{T}}\ddot{\mathbf{q}} = 0, \tag{16}$$

and for which the force restriction $\lambda_N > 0$ has to be verified afterwards. Eqs. (15) and (16) completely describe the dynamics of the system for the state enduring contact with slip and will be used in the following to perform the stability analysis.

Within the framework of linear stability analysis, we assume the solution $\mathbf{q}(t)$ of Eqs. (15) and (16) to be composed of the equilibrium $\mathbf{q}_0 = \text{const.}$ and small superimposed deviations $\mathbf{y}(t)$. In the same manner, the overall normal force $\lambda_N(t)$ is assumed to consist of a nominal force $\lambda_{N0} = \text{const.}$ together with small deviations $v_N(t)$,

$$\mathbf{q}(t) = \mathbf{q}_0 + \mathbf{y}(t), \quad \lambda_N(t) = \lambda_{N0} + v_N(t). \tag{17}$$

The equilibrium point $(\mathbf{q}_0, \lambda_{N0})$ as one solution of the equations of motion is now determined by putting $\dot{\mathbf{q}}_0 = \ddot{\mathbf{q}}_0 = 0$ into Eqs. (15) and (16), which results in

$$\mathbf{K}\mathbf{q}_0 - (\mathbf{w}_N - \mu \mathbf{W}_T \mathbf{e}_{T0})\lambda_{N0} = 0 \quad \text{with } \mathbf{e}_{T0} = \frac{\boldsymbol{\chi}_T}{\|\boldsymbol{\chi}_T\|}, \tag{18}$$

$$g_{N0} = \mathbf{w}_N^{\mathrm{T}}\mathbf{q}_0 + \hat{a} = 0, \tag{19}$$

from which the values of $(\mathbf{q}_0, \lambda_{N0})$ can be calculated. One further recognizes that the last two equations in Eq. (16) are identically fulfilled for the equilibrium point. With $\mathbf{q}_0$ from Eqs. (18) and (19), the 61 constant modal amplitudes for stationary sliding are known. They depend on the creep direction $\mathbf{e}_{T0}$.

The Newton–Euler equations (15) are now linearized around the equilibrium position $(\mathbf{q}_0, \lambda_{N0})$. Note that the only nonlinearity in the system stems from the direction of the friction force for sliding which is determined by the direction $\mathbf{e}_T(\dot{\mathbf{q}})$ of the relative velocity in the contact point. By using Eq. (17), linearization yields

$$\mathbf{M}\ddot{\mathbf{y}} + \mathbf{D}\dot{\mathbf{y}} + \mathbf{K}\mathbf{y} - (\mathbf{w}_N - \mu \mathbf{W}_T \mathbf{e}_{T0})v_N + \mu\lambda_{N0}\mathbf{W}_T \left(\frac{\partial \mathbf{e}_T}{\partial \dot{\mathbf{q}}}\right)_0 \dot{\mathbf{y}} = 0, \tag{20}$$

with the changes $\partial/\partial\dot{\mathbf{q}}$ in the sliding direction $\mathbf{e}_T$ from Eq. (15), evaluated at the equilibrium

$$\left(\frac{\partial \mathbf{e}_T}{\partial \dot{\mathbf{q}}}\right)_0 = \left(\frac{\mathbb{1}}{\|\boldsymbol{\chi}_T\|} - \frac{\boldsymbol{\chi}_T \boldsymbol{\chi}_T^{\mathrm{T}}}{\|\boldsymbol{\chi}_T\|^3}\right)\mathbf{W}_T^{\mathrm{T}} = \frac{1}{\|\boldsymbol{\chi}_T\|}(\mathbb{1} - \mathbf{e}_{T0}\mathbf{e}_{T0}^{\mathrm{T}})\mathbf{W}_T^{\mathrm{T}} =: \mathbf{R}\mathbf{W}_T^{\mathrm{T}} \quad \text{with } \mathbf{R} = \mathbf{R}^{\mathrm{T}} \text{ psd.} \tag{21}$$

Eqs. (20) and (21) together yield

$$\mathbf{M}\ddot{\mathbf{y}} + (\mathbf{D} + \mu\lambda_{N0}\mathbf{W}_T\mathbf{R}\mathbf{W}_T^{\mathrm{T}})\dot{\mathbf{y}} + \mathbf{K}\mathbf{y} - (\mathbf{w}_N - \mu\mathbf{W}_T\mathbf{e}_{T0})v_N = 0, \tag{22}$$

in which we abbreviate the terms in front of $\dot{\mathbf{y}}$ and v_N as

$$\mathbf{H} := \mathbf{D} + \mu\lambda_{N0}\mathbf{W}_T\mathbf{R}\mathbf{W}_T^{\mathrm{T}}, \quad \mathbf{w}_R := \mathbf{w}_N - \mu\mathbf{W}_T\mathbf{e}_{T0} \tag{23}$$

to arrive with the Newton–Euler equations in the form

$$\mathbf{M}\ddot{\mathbf{y}} + \mathbf{H}\dot{\mathbf{y}} + \mathbf{K}\mathbf{y} - \mathbf{w}_R v_N = 0 \tag{24}$$

with constant, symmetric and positive definite matrices $\mathbf{M}$, $\mathbf{H}$ and $\mathbf{K}$. In a final step, the deviations v_N in the normal force are eliminated from Eq. (24), which is performed with the help of the equality constraints in Eq. (16) and which basically follows the elimination procedure for non-perfect constraints introduced in Refs. [21,22]. With $\mathbf{q}(t)$ from Eq. (17), the last equation in Eq. (16) becomes

$$\dot{\gamma}_N = \mathbf{w}_N^{\mathrm{T}}\ddot{\mathbf{q}} = \mathbf{w}_N^{\mathrm{T}}\ddot{\mathbf{y}} = 0. \tag{25}$$

The Newton–Euler equations (24) are now solved for $\ddot{\mathbf{y}}$,

$$\ddot{\mathbf{y}} = \mathbf{M}^{-1}\mathbf{w}_R v_N - \mathbf{M}^{-1}(\mathbf{H}\dot{\mathbf{y}} + \mathbf{K}\mathbf{y}), \tag{26}$$

and then substituted into Eq. (25). The resulting equation

$$\mathbf{w}_N^{\mathrm{T}}\mathbf{M}^{-1}\mathbf{w}_R v_N = \mathbf{w}_N^{\mathrm{T}}\mathbf{M}^{-1}(\mathbf{H}\dot{\mathbf{y}} + \mathbf{K}\mathbf{y}) \tag{27}$$

can then be solved for v_N. By abbreviating the term in front of v_N as

$$d := \mathbf{w}_N^{\mathrm{T}}\mathbf{M}^{-1}\mathbf{w}_R, \tag{28}$$

the deviations v_N in the normal force become

$$v_N = \frac{1}{d}\mathbf{w}_N^{\mathrm{T}}\mathbf{M}^{-1}(\mathbf{H}\dot{\mathbf{y}} + \mathbf{K}\mathbf{y}). \tag{29}$$

This expression is finally re-substituted into Eq. (24), which yields

$$\mathbf{M}\ddot{\mathbf{y}} + \mathbf{H}\dot{\mathbf{y}} + \mathbf{K}\mathbf{y} - \frac{1}{d}\mathbf{w}_R\mathbf{w}_N^{\mathrm{T}}\mathbf{M}^{-1}(\mathbf{H}\dot{\mathbf{y}} + \mathbf{K}\mathbf{y}) = 0 \tag{30}$$

or, after having collected the velocity and displacement dependent terms,

$$\mathbf{M}\ddot{\mathbf{y}} + \left(\mathbb{1} - \frac{1}{d}\mathbf{w}_R\mathbf{w}_N^{\mathrm{T}}\mathbf{M}^{-1}\right)\mathbf{H}\dot{\mathbf{y}} + \left(\mathbb{1} - \frac{1}{d}\mathbf{w}_R\mathbf{w}_N^{\mathrm{T}}\mathbf{M}^{-1}\right)\mathbf{K}\mathbf{y} = 0. \tag{31}$$

With the abbreviations for d in Eq. (28), $\mathbf{w}_R$ and $\mathbf{H}$ in Eq. (23) and $\mathbf{R}$ in Eq. (21), the equations of motion (31) have the structure

$$\mathbf{M}\ddot{\mathbf{y}} + \mathbf{B}(\mu, \mathbf{e}_{T0}, \|\boldsymbol{\chi}_T\|)\dot{\mathbf{y}} + \mathbf{C}(\mu, \mathbf{e}_{T0})\mathbf{y} = 0. \tag{32}$$

We recall that the only nonlinearity in the system is due to the sliding direction $\mathbf{e}_T(\dot{\mathbf{q}})$. The linearization of this nonlinear term contributes to both the stiffness and damping matrix in Eq. (32), which destroys their symmetry and opens the possibility for dynamic instabilities. The (linear) stability of the stationary run is determined by the eigenvalues of this linearized system (32). The artificial twofold null-eigenvalue which occurs due to the implicitly still present constraint (16) can be disregarded in the stability analysis.

Note, however, that even for the friction*less* case ($\mu = 0$ and consequently $\mathbf{H} = \mathbf{D}$, $\mathbf{w}_R = \mathbf{w}_N$ by Eq. (23)), the damping and stiffness matrices in Eq. (31) may still be non-symmetric. In contrast to the terms resulting from the Coulomb friction, these asymmetries are artificial and caused by the various steps that have been necessary to eliminate the constraint force v_N. These unessential asymmetries, as well as the aforementioned null-eigenvalue can be removed by passing to a new set of minimal coordinates $\mathbf{z} \in \mathbb{R}^{f-1}$ which implicitly fulfills the constraint (16), see again Refs. [21,22] but also Ref. [8] for a clear structural interpretation of the necessary steps,

$$\mathbf{y} = \mathbf{Q}\mathbf{z} \;\Rightarrow\; g_N = \mathbf{w}_N^{\mathrm{T}}\mathbf{q} + \hat{a} = \mathbf{w}_N^{\mathrm{T}}(\mathbf{q}_0 + \mathbf{y}) + \hat{a} = \mathbf{w}_N^{\mathrm{T}}\mathbf{y} = \mathbf{w}_N^{\mathrm{T}}\mathbf{Q}\mathbf{z} \equiv 0\ \forall \mathbf{z} \;\Rightarrow\; \mathbf{w}_N^{\mathrm{T}}\mathbf{Q} = 0. \tag{33}$$

This finally provides us with the well-known annihilator condition $\mathbf{w}_N^{\mathrm{T}}\mathbf{Q} = 0$. As in Eq. (11), the reduction of the equations of motion (30) to this set of new coordinates $\mathbf{z}$ is performed on the virtual work of the system. In the resulting equation

$$\mathbf{Q}^{\mathrm{T}}\mathbf{M}\mathbf{Q}\ddot{\mathbf{z}} + \mathbf{Q}^{\mathrm{T}}\mathbf{H}\mathbf{Q}\dot{\mathbf{z}} + \mathbf{Q}^{\mathrm{T}}\mathbf{K}\mathbf{Q}\mathbf{z} - \frac{1}{d}\mathbf{Q}^{\mathrm{T}}\mathbf{w}_R\mathbf{w}_N^{\mathrm{T}}\mathbf{M}^{-1}(\mathbf{H}\mathbf{Q}\dot{\mathbf{z}} + \mathbf{K}\mathbf{Q}\mathbf{z}) = 0 \tag{34}$$

the term $\mathbf{w}_R$ from Eq. (23) is re-substituted, which yields together with $\mathbf{Q}^{\mathrm{T}}\mathbf{w}_N = 0$ the final form

$$\mathbf{Q}^{\mathrm{T}}\mathbf{M}\mathbf{Q}\ddot{\mathbf{z}} + \mathbf{Q}^{\mathrm{T}}\mathbf{H}\mathbf{Q}\dot{\mathbf{z}} + \mathbf{Q}^{\mathrm{T}}\mathbf{K}\mathbf{Q}\mathbf{z} + \frac{\mu}{d}\mathbf{Q}^{\mathrm{T}}(\mathbf{W}_T\mathbf{e}_{T0}\mathbf{w}_N^{\mathrm{T}}\mathbf{M}^{-1})(\mathbf{H}\mathbf{Q}\dot{\mathbf{z}} + \mathbf{K}\mathbf{Q}\mathbf{z}) = 0. \tag{35}$$

Obviously, the resulting matrices in the first three summands are symmetric, whereas non-removable asymmetries may occur in the fourth summand due to the term $\mathbf{W}_T\mathbf{e}_{T0}\mathbf{w}_N^{\mathrm{T}}\mathbf{M}^{-1}$. For the frictionless case ($\mu = 0$), constraint (16) becomes ideal and the fourth summand in Eq. (35) drops out, leading to symmetrical equations of motion as expected.

Fig. 8 shows the results of the stability analysis (18), (19), (32) for all four wheels of the leading bogie, which have been computed with the eigenmodes of an 800 mm wheel with fixed center nodes. The radial direction in the stability charts corresponds to the chosen friction coefficient μ, whereas the azimuth angle addresses the nominal creep direction $\mathbf{e}_{T0}$ which has been varied numerically. The magnitude of the nominal creep $\|\boldsymbol{\chi}_T\|$ has been taken as computed from the multibody simulation (Table 2) and has not been varied. Points in the stability charts, which correspond to the states calculated from the multibody simulation, are marked by black stars. For the leading inner wheel, these points correspond to the friction coefficient and creep velocities in Table 2. Points for which the real part of one of the eigenvalues of Eq. (31) is strictly positive are marked in dark gray and correspond to unstable stationary driving states. The points in light gray indicate asymptotically stable states. We infer from the upper left stability chart in Fig. 8 that the leading inner wheel is prone to instability, as the actual calculated states from the multibody simulation enter the unstable region already for small friction coefficients. Contrary, the inner second wheel is safely within the stability region. The results for the leading outer wheel are doubtful, because the flanging in the simulation is only modelled as a single but not as a more realistic double contact. The results of the outer second wheel indicate that the stationary motion is stable, at least in theory. However, uncertainties in the model and irregularities in the real system make this result questionable as the distance to the stability border is not large enough to ensure stability in praxis. These theoretical results agree with the measurements of Section 2.

Fig. 9 shows the stability charts for the leading inner wheel calculated for various wheel diameters. It can be seen that the instability region for diameters larger than 800 mm is located at the left-hand side of the diagram, whereas it is mostly on the right-hand side for diameters of 780 mm, which implies a stable stationary motion for this case. Accordingly, reprofiling of the leading inner wheel may in the long term cause the squeal phenomenon to cease. The sudden disappearance of squeal has indeed been observed in the measurements which lasted several months. Self-excited oscillations occur almost always at a frequency close to an

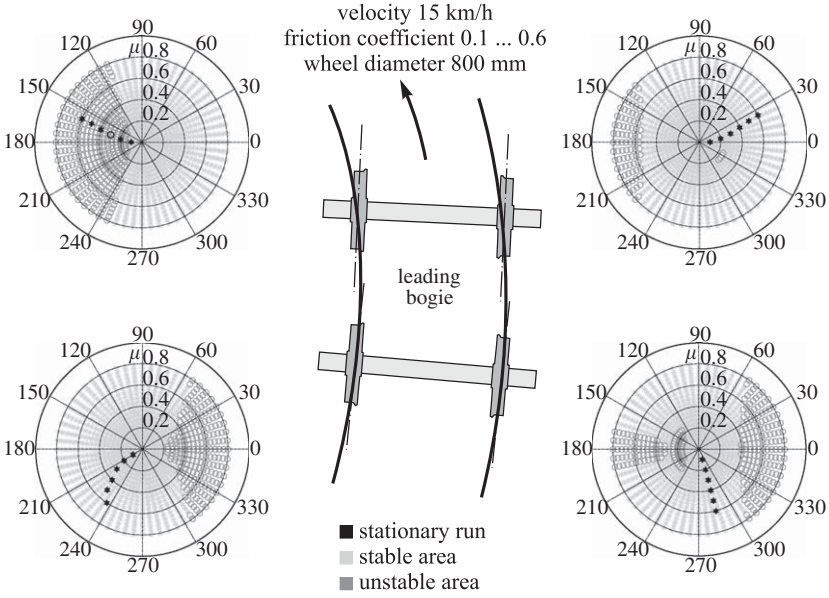

Fig. 8. Stability charts for the four wheels of the leading bogie.

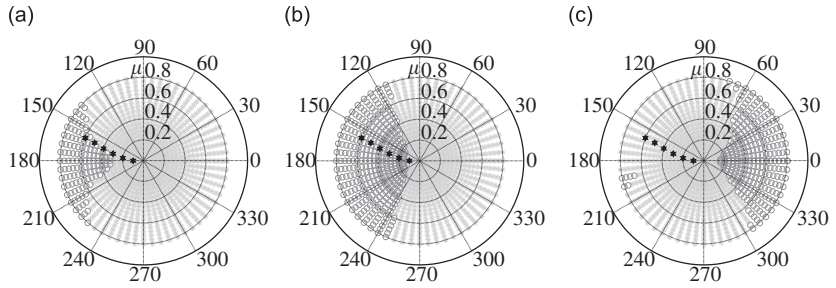

Fig. 9. Stability charts for the leading inner wheel of the leading bogie for various wheel diameters: (a) diameter 820 mm, (b) diameter 800 mm and (c) diameter 780 mm.

eigenfrequency of the system, as they are normally born from Hopf bifurcations [23]. As stated before, a coupling between degrees of freedom in normal and tangential direction of the contact are necessary for friction-induced vibrations with a constant friction coefficient. The normal degree of freedom causes a varying normal contact force, which induces a varying friction force exciting the system in tangential direction. This implies that *at least* two degrees of freedom need to be present. The intensity of the coupling is strong if the eigenfrequencies of the normal and tangential direction are close to each other as this facilitates the necessary exchange of energy. The three modes depicted on the right-hand side in Fig. 4 have almost the same frequencies for large wheel diameters, but these frequencies separate from one another as the wheel diameter is reduced. We are led to believe that for wheel diameters 820 and 800 mm the modes 31–32 and 33–34 share the variation of the normal contact force, whereas for 780 mm just only mode 31–32 participates, which might explain the transition of the stability region from the left- to the right-hand sides in Fig. 9. The precise mechanism behind this phenomenon is still an open question. Moreover, the possibility of squeal at a frequency of about 4400 Hz for even smaller wheel diameters due to the approach of modes 33–34, 42–43 and 50–51 needs to be studied. All three modes, 31–32, 33–34, 35–36, are essential for squeal to appear at a wheel diameter of 800 mm. If one of these modes is removed from the numerical calculation, the squeal mechanism ceases to exist.

We finally want to mention that isotropic Stribeck effects could be taken into account by making the friction coefficient μ dependent on the sliding velocity, $\mu : \mathbb{R}_0^+ \to \mathbb{R}$, $v \to \mu(v)$ with $v(\boldsymbol{\gamma}_T) = \|\boldsymbol{\gamma}_T\|$. In this way, the slope of the friction curve taken at the nominal creep, $\mu'(v_0) = \mu'(\|\boldsymbol{\chi}_T\|)$, would enter the linearization process described above and would lead to an additional term in Eq. (20). In particular, $\mathbf{R}$ would have to be replaced by $\hat{\mathbf{R}} := \mathbf{R} + (\mu'(v_0)/\mu(v_0))\mathbf{e}_{T0}\mathbf{e}_{T0}^{\mathrm{T}}$ in Eqs. (22) et seqq., as basic calculations show. The instability regions in Figs. 8 and 9 depend continuously on the eigenvalues of the system (32), and the eigenvalues depend continuously on the system parameters. As a consequence, the instability regions, computed for a constant friction coefficient ($\mu'(v_0) \equiv 0$) as done in the figures above, would not change much for small slopes in the friction curves ($\|\mu'(v_0)/\mu(v_0)\| \ll 1/v_0$). Instability of the system is therefore structurally stable within certain bounds of $\mu'(v_0)$.

7. Numerical simulation of self-excitation

In the linear stability analysis of Section 6 it has been shown that, in particular, the stationary run of the inner leading wheel can become unstable. However, it is from the linear analysis still unknown whether this instability leads to a bounded oscillatory motion and how this oscillatory motion would look like. To this end, the nonlinear differential inclusions of the reduced model described in Section 5 are numerically simulated. The simulations have been conducted with a research code dedicated to the simulation of mechanical systems with impact and friction, see Ref. [30] and in particular Ref. [9] for a full account. The time integration is performed with a half-implicit index-2-solver and the inequalities are solved with nonlinear projections [9]. Both are in detail reviewed in this section in a form tailored for the curve squealing problem.

In order to prepare the equations of motion (13), (14), (8), (9) for numerical integration, they have to be displayed in an utmost compact and concise form, together with a unified structure for the contact laws. In a

first step, the Newton–Euler equations (13) and kinematics (14) are left as they have been

$$\mathbf{M}\ddot{\mathbf{q}} + \mathbf{D}\dot{\mathbf{q}} + \mathbf{K}\mathbf{q} - \mathbf{w}_N\lambda_N - \mathbf{W}_T\boldsymbol{\lambda}_T = 0, \tag{36}$$

$$g_N = \mathbf{w}_N^{\mathrm{T}}\mathbf{q} + \hat{a}, \quad \gamma_N = \mathbf{w}_N^{\mathrm{T}}\dot{\mathbf{q}}, \quad \boldsymbol{\gamma}_T = \mathbf{W}_T^{\mathrm{T}}\dot{\mathbf{q}} + \boldsymbol{\chi}_T, \tag{37}$$

but the contact laws (8) and (9) are re-formulated as normal cone inclusions. The latter require to specify the (convex) sets $\mathscr{C}_N$ and $\mathscr{C}_T$ of negative admissible normal and tangential forces $-\lambda_N$ and $-\boldsymbol{\lambda}_T$, which are according to Eqs. (8) and (9) given by

$$\mathscr{C}_N := \mathbb{R}_0^- \subset \mathbb{R}, \quad \mathscr{C}_T(\lambda_N) := \mu\lambda_N\mathscr{B}_2 \subset \mathbb{R}^2 \quad \text{with } \mathscr{B}_2 = \{\mathbf{a} \in \mathbb{R}^2 | \|\mathbf{a}\| \leqslant 1\}, \tag{38}$$

and which take into account the restrictions $\lambda_N \geqslant 0$ and $\|\boldsymbol{\lambda}_T\| \leqslant \mu\lambda_N$ by the conditions $-\lambda_N \in \mathscr{C}_N$ and $-\boldsymbol{\lambda}_T \in \mathscr{C}_T(\lambda_N)$. It is now possible to express the two cases for $g_N = 0$ in the normal contact law (8) and the whole tangential contact law (9) by one normal cone inclusion each, such that the complete contact laws are represented by

$$\begin{cases} g_N > 0 & \Rightarrow -\lambda_N = 0, \\ g_N = 0 & \Rightarrow \gamma_N \in \mathscr{N}_{\mathscr{C}_N}(-\lambda_N), \end{cases} \quad \boldsymbol{\gamma}_T \in \mathscr{N}_{\mathscr{C}_T(\lambda_N)}(-\boldsymbol{\lambda}_T). \tag{39}$$

For a convex set $\mathscr{C} \subset \mathbb{R}^m$, the normal cone $\mathscr{N}_{\mathscr{C}}(\mathbf{x}) \subset \mathbb{R}^m$ at a point $\mathbf{x} \in \mathscr{C}$ is defined as to consist of all vectors $\mathbf{y}$, for which the variational inequality $\mathbf{y}^{\mathrm{T}}(\mathbf{x}^\star - \mathbf{x}) \leqslant 0$ holds for all $\mathbf{x}^\star \in \mathscr{C}$. It therefore consists of all vectors $\mathbf{y}$ which do not form an acute angle with any line segment starting at $\mathbf{x} \in \mathscr{C}$ and endpoint $\mathbf{x}^\star$ in $\mathscr{C}$. Note in particular that $\mathscr{N}_{\mathscr{C}}(\mathbf{x}) = \{0\}$ if $\mathbf{x}$ is in the interior of $\mathscr{C}$, which covers the cases $\gamma_N = 0$ and $\boldsymbol{\gamma}_T = 0$ in Eqs. (8) and (9) when strong inequalities are applied on the associated conditions for λ_N and $\boldsymbol{\lambda}_T$. The reader should check by himself that Eq. (39) is indeed an equivalent representation of the contact laws (8) and (9).

We introduce now some abbreviations to write the Newton–Euler equations (36) and kinematics (37) in a more compact form. In particular, we distinguish explicitly between position and velocity coordinates, and we set all terms which are associated with the normal direction N into the same vector-matrix notation as the tangential terms T. With

$$\mathbf{u} := \dot{\mathbf{q}}, \quad \mathbf{h}(\mathbf{q}, \mathbf{u}) := -\mathbf{D}\dot{\mathbf{q}} - \mathbf{K}\mathbf{q}, \quad \boldsymbol{\gamma}_N := \gamma_N, \quad \boldsymbol{\lambda}_N := \lambda_N, \quad \mathbf{W}_N := \mathbf{w}_N, \quad \boldsymbol{\chi}_N := 0, \tag{40}$$

Eqs. (36) and (37) can be written together as

$$\mathbf{M}\dot{\mathbf{u}} - \mathbf{h}(\mathbf{q}, \mathbf{u}) - \sum_{i \in \{N,T\}} \mathbf{W}_i\boldsymbol{\lambda}_i = 0, \quad g_N = \mathbf{w}_N^{\mathrm{T}}\mathbf{q} + \hat{a}, \quad \boldsymbol{\gamma}_i = \mathbf{W}_i^{\mathrm{T}}\mathbf{u} + \boldsymbol{\chi}_i \quad (i \in \{N, T\}). \tag{41}$$

The distinction of cases for g_N, which is still present in the normal contact law and which affects via $\mathscr{C}_T(\lambda_N)$ also the tangential contact law, can be removed from Eq. (39) by introducing the index set

$$\mathscr{H}(\mathbf{q}) := \begin{cases} \emptyset & \text{if } \mathbf{w}_N^{\mathrm{T}}\mathbf{q} + \hat{a} > 0, \\ \{N, T\} & \text{if } \mathbf{w}_N^{\mathrm{T}}\mathbf{q} + \hat{a} = 0, \end{cases} \tag{42}$$

which determines by the second equation in Eq. (41) whether the contact is open or closed and whether contact forces have to be considered or not. We therefore may now write the two remaining equations from Eq. (41) together with the remaining conditions from Eq. (39) as

$$\mathbf{M}\dot{\mathbf{u}} - \mathbf{h}(\mathbf{q}, \mathbf{u}) - \sum_{i \in \mathscr{H}} \mathbf{W}_i\boldsymbol{\lambda}_i = 0, \quad \boldsymbol{\gamma}_i = \mathbf{W}_i^{\mathrm{T}}\mathbf{u} + \boldsymbol{\chi}_i, \quad \boldsymbol{\gamma}_i \in \mathscr{N}_{\mathscr{C}_i}(-\boldsymbol{\lambda}_i) \quad (i \in \{N, T\}). \tag{43}$$

The equations of motion, previously expressed by Eqs. (13), (14), (8), (9), are now fully determined by Eq. (43), the index set (42) and the sets of admissible forces (38).

As already mentioned, the differential inclusions (43) completely describe the motion of the system with all the different states and transitions between them, except of the impact. An impact due to a collision of the wheel against the rail is a highly improbable event for curve squealing, because it would require a preceding lift-off of the contact. Nevertheless, the differential inclusions (43) have even then to be extended to impacts because of numerical reasons: An index-1-approach would require to re-formulate the contact laws on acceleration level, which would lead to additional index sets like the one in Eq. (42), together with additional

tolerances to decide when an index is changed numerically. This affects in particular the slip-stick transition, for which zero tangential relative velocity has then to be detected numerically. Since the friction model is a spatial one, root-finding cannot be applied but has to be replaced by a norm condition and succeeding projection to null-velocity (which already is a velocity jump and hence an impact from the mechanical point of view). All that would make the numerical scheme unreliable and prone to numerical drift. The much better approach is to leave the contact laws on velocity level as in Eq. (43) and to discretize the Newton–Euler equations in integrated form on velocity-impulse level, which corresponds with an index-2-approach. The velocity-impulse level, however, is the level at which impacts are resolved, and numerics therefore naturally asks for properly addressing the impact problem. We therefore state (43) on velocity-impulse level by integration over *any* compact time interval $I=[t_A,t_E]$ and *additionally* include the system's impact dynamics in the form

$$\int_I \mathbf{M}\mathrm{d}\mathbf{u}-\mathbf{h}(\mathbf{q},\mathbf{u})\,\mathrm{d}t-\sum_{i\in\mathscr{H}}\mathbf{W}_i\mathrm{d}\boldsymbol{\Delta}_i=0,\quad \boldsymbol{\gamma}_i^{\pm}=\mathbf{W}_i^{\mathrm{T}}\mathbf{u}^{\pm}+\boldsymbol{\chi}_i,\quad (1+\varepsilon_i)\boldsymbol{\gamma}_i^{-}+\int_I \mathrm{d}\boldsymbol{\gamma}_i\in\mathscr{N}_{\int_I \mathrm{d}\mathscr{A}_i}\left(\int_I -\mathrm{d}\boldsymbol{\Delta}_i\right). \tag{44}$$

Within this setting, the velocities $\mathbf{u}(t)$ are understood as functions of special bounded variations, allowing for a countable number of discontinuities and for the right and left limit $\mathbf{u}^+(t)$ and $\mathbf{u}^-(t)$ of $\mathbf{u}(t)$ to exist at every t. Because of the discontinuities occurring in $\mathbf{u}(t)$, its derivative must not be understood in the classical sense. Instead, the differential measure [24] $\mathrm{d}\mathbf{u}=\dot{\mathbf{u}}\,\mathrm{d}t+(\mathbf{u}^+-\mathbf{u}^-)\,\mathrm{d}\eta$ has to be used, to which the Lebesgue measure $\mathrm{d}t$ and the Dirac point measure $\mathrm{d}\eta$ contribute. The latter is needed to gain back by integration the discontinuities in $\mathbf{u}(t)$, $\int_{\{t\}}\mathrm{d}\mathbf{u}=\mathbf{u}^+(t)-\mathbf{u}^-(t)$. All properties of $\mathbf{u}(t)$ are passed by the second equation in Eq. (43) to the relative velocities $\boldsymbol{\gamma}_i$, for which $\mathrm{d}\boldsymbol{\gamma}_i=\dot{\boldsymbol{\gamma}}_i\,\mathrm{d}t+(\boldsymbol{\gamma}_i^+-\boldsymbol{\gamma}_i^-)\,\mathrm{d}\eta$ consequently holds. In the same manner, the finite forces $\boldsymbol{\lambda}_i$ from Eq. (43) have to be replaced in Eq. (44) by their associated force impulse measures $\mathrm{d}\boldsymbol{\Delta}_i=\boldsymbol{\lambda}_i\,\mathrm{d}t+\boldsymbol{\Lambda}_i\,\mathrm{d}\eta$, in which the impulsive forces $\boldsymbol{\Lambda}_i$, needed to balance the discontinuities of $\mathbf{u}(t)$ at the impacts, are contained. Accordingly, the force reservoirs $\mathscr{C}_i$ are to be replaced by $\mathrm{d}\mathscr{A}_i=\mathscr{C}_i\,\mathrm{d}t+\mathscr{D}_i\,\mathrm{d}\eta$. Finally, the generalized coordinates $\mathbf{q}(t)$ have now to be understood as the integrals of the velocity functions $\mathbf{u}(t)$ and become by integration absolutely continuous functions of time. The most challenging task in setting up (44) is certainly the consistent extension of the contact laws to an expression that in addition includes some well-defined impact laws and that is displayed in the last formula of Eq. (44). Each normal cone inclusion is equipped with a coefficient of restitution ε_i with the usual values $\varepsilon_i\in[0,1]$. It will be shown next that the impact-free motion (43) is indeed still contained in Eq. (44), and how the equations for resolving the impacts look like.

For motion without impacts, the Dirac measure $\mathrm{d}\eta$ does not contribute to Eq. (44). As a consequence, the velocities become continuous, $\mathbf{u}^+=\mathbf{u}^-=\mathbf{u}$, $\boldsymbol{\gamma}_i^+=\boldsymbol{\gamma}_i^-=\boldsymbol{\gamma}_i$, and Eq. (44) reduces to

$$\int_I \mathbf{M}\dot{\mathbf{u}}\,\mathrm{d}t-\mathbf{h}(\mathbf{q},\mathbf{u})\,\mathrm{d}t-\sum_{i\in\mathscr{H}}\mathbf{W}_i\boldsymbol{\lambda}_i\,\mathrm{d}t=0,\quad \boldsymbol{\gamma}_i=\mathbf{W}_i^{\mathrm{T}}\mathbf{u}+\boldsymbol{\chi}_i,\quad (1+\varepsilon_i)\boldsymbol{\gamma}_i+\int_I \dot{\boldsymbol{\gamma}}_i\mathrm{d}t\in\mathscr{N}_{\int_I \mathscr{C}_i\,\mathrm{d}t}\left(\int_I -\boldsymbol{\lambda}_i\,\mathrm{d}t\right), \tag{45}$$

which verifies already the second equation in Eq. (43). The first equation in Eq. (43) can be obtained from the first equation in Eq. (45) by the fact that Eq. (44) has been required to hold for any time interval I. Equivalently, one pre-multiplies the Newton–Euler equations in Eq. (45) by test functions and applies the fundamental lemma of variational calculus to obtain the desired result. In order to extract the normal cone inclusion in Eq. (43) from the last expression in Eq. (45), we let $I\to 0$ with $\int_I \dot{\boldsymbol{\gamma}}_i\,\mathrm{d}t\to 0$ as an immediate consequence. Furthermore, both the set $\mathscr{C}_i\,\mathrm{d}t$ and the force $-\boldsymbol{\lambda}_i\,\mathrm{d}t$ scale uniformly to zero by this process, such that $(1+\varepsilon_i)\boldsymbol{\gamma}_i\in\mathscr{N}_{\mathscr{C}_i}(-\boldsymbol{\lambda}_i)$ is obtained for the limit. We finally divide both sides of this inclusion by the positive number $(1+\varepsilon_i)>0$, which does not alter the right-hand side, because $\mathscr{N}_{\mathscr{C}_i}$ is a cone.

In order to extract the impact dynamics from Eq. (44), one takes for integration one single instant in time, $I=\{t\}$, such that the Lebesgue measure $\mathrm{d}t$ cannot contribute and only the Dirac measure $\mathrm{d}\eta$ survives. This yields

$$\mathbf{M}(\mathbf{u}^+-\mathbf{u}^-)-\sum_{i\in\mathscr{H}}\mathbf{W}_i\boldsymbol{\Lambda}_i=0,\quad \boldsymbol{\gamma}_i^{\pm}=\mathbf{W}_i^{\mathrm{T}}\mathbf{u}^{\pm}+\boldsymbol{\chi}_i,\quad \boldsymbol{\gamma}_i^{+}+\varepsilon_i\boldsymbol{\gamma}_i^{-}\in\mathscr{N}_{\mathscr{D}_i}(-\boldsymbol{\Lambda}_i). \tag{46}$$

We call the first expression in Eq. (46) the Newton–Euler equations for impacts. They contain the impulsive forces $\boldsymbol{\Lambda}_i$ that are necessary to realize the jump $\mathbf{u}^+-\mathbf{u}^-$ in the generalized velocities. The second equation in

Eq. (46) expresses, as in Eq. (44), the kinematic transformation between generalized and contact relative velocities. Finally, the normal cone inclusions on the right of Eq. (46) constitute the impact laws. In this particular form, we call them the standard inequality impact laws of Newton type for frictional contacts. They are discussed in detail for the planar case in Ref. [25]. The associated reservoirs for the impulsive forces are $\mathscr{D}_N = \mathbb{R}_0^-$ and $\mathscr{D}_T(\Lambda_N) = \mu\Lambda_N\mathscr{B}_2$.

The design of reliable and accurate integration algorithms for measure differential inclusions of type (44) is today one of the core activities in non-smooth mechanics. The so-called time stepping methods, which allow for simultaneously handling the impact-free motion and the impacts, are difference schemes on velocity level within which all inequalities together with the associated switching events are evaluated. In contrast to event-driven integration, which aims at resolving the switching events by re-initialization procedures at the boundary of the integration steps, are those events left in the interior such that multiple switching and even accumulation points can be processed. To the best of our knowledge, time stepping for inequality problems in dynamics has been introduced for the first time by Moreau [26]. His algorithm, which we consider still as the most fundamental one, consists of a midpoint rule for the positions and an Euler backwards step for the velocities, and has been applied here for integrating the measure differential inclusions (44). To perform one integration step, the following problem has to be addressed: For given initial time t_A, initial positions $\mathbf{q}_A = \mathbf{q}(t_A)$ and initial velocities $\mathbf{u}_A = \mathbf{u}(t_A)$, determine approximates $\mathbf{q}_E$ and $\mathbf{u}_E$ of the endpoint positions $\mathbf{q}(t_E)$ and endpoint velocities $\mathbf{u}(t_E)$ at timet_E. In order to apply Moreau's time-stepping scheme one has to proceed as follows, see Ref. [27] for details and helpful comments:

1. Choose a time step Δt and calculate the midpoint $t^M := t^A + \frac{1}{2}\Delta t$ and the endpoint $t^E := t^A + \Delta t$.
2. Calculate the midpoint positions $\mathbf{q}^M := \mathbf{q}^A + \frac{1}{2}\Delta t\mathbf{u}^A$.
3. Compute $\mathbf{h}(\mathbf{q}^M, \mathbf{u}^A)$ and the index set $\mathscr{H}(\mathbf{q}^M)$ according to Eq. (42). For numerical reasons, the condition $\mathbf{w}_N^{\mathrm{T}}\mathbf{q} + \hat{a} = 0$ is here replaced by $\mathbf{w}_N^{\mathrm{T}}\mathbf{q} + \hat{a} \leqslant 0$ to resolve also negative contact gaps which occur when the bodies numerically interpenetrate each other.
4. Compute $\mathbf{u}^E$ from the discretized inclusion problem (44),
$$\mathbf{M}(\mathbf{u}^E - \mathbf{u}^A) - \mathbf{h}\Delta t - \sum_{i\in\mathscr{H}} \mathbf{W}_i\Delta_i = 0, \quad \gamma_i^A = \mathbf{W}_i^{\mathrm{T}}\mathbf{u}^A + \boldsymbol{\chi}_i, \quad \gamma_i^E = \mathbf{W}_i^{\mathrm{T}}\mathbf{u}^E + \boldsymbol{\chi}_i, \quad \gamma_i^E + \varepsilon_i\gamma_i^A \in \mathscr{N}_{\mathscr{A}_i}(-\boldsymbol{\Delta}_i). \tag{47}$$
For the discretization, the terms $\mathrm{d}\mathbf{u}$, $\mathrm{d}\gamma_i$, $\mathrm{d}\boldsymbol{\Delta}_i$, $\mathrm{d}\mathscr{A}_i$ and $\mathrm{d}t$ in Eq. (44) have been approximated by $\mathbf{u}^E - \mathbf{u}^A$, $\gamma_i^E - \gamma_i^A$, $\boldsymbol{\Delta}_i$, $\mathscr{A}_i$ and Δt. Furthermore, the upper indices + and − have been replaced by the initial time and end time indices A and E. The sets $\mathscr{A}_i$ in Eq. (47) are $\mathscr{A}_N = \mathbb{R}_0^-$ and $\mathscr{A}_T(\Delta_N) = \mu\Delta_N\mathscr{B}_2$.
5. Compute the endpoint positions $\mathbf{q}^E := \mathbf{q}^M + 1/2\Delta t \cdot \mathbf{u}^E$ with $\mathbf{u}^E$ from Eq. (47).

The discretization scheme introduced above is of first order and requires therefore relatively small step sizes. A scheme which allows for a higher-order integration within the intervals of smooth motion and which is equipped with a step width control can be obtained from the above by extrapolation, as originally presented in Ref. [9].

There are many approaches suggested in the literature on how to solve the inclusion problem (47). The most fundamental one is in our opinion the proximal point method combined with a blockwise Gauss–Seidel iteration, from which most of the other approaches can be extracted and interpreted as special cases, see Refs. [28,29]. In order to set up the required structure, the discretized Newton–Euler equations in Eq. (47) are solved for $\mathbf{u}^E$,

$$\mathbf{u}^E = \mathbf{u}^A + \mathbf{M}^{-1}\mathbf{h}\Delta t + \sum_{i\in\mathscr{H}} \mathbf{M}^{-1}\mathbf{W}_i\boldsymbol{\Delta}_i \tag{48}$$

and substituted into the term $\gamma_i^E + \varepsilon_i\gamma_i^A$ built from the second and third equation in Eq. (47). In the resulting equation

$$\gamma_i^E + \varepsilon_i\gamma_i^A = \mathbf{W}_i^{\mathrm{T}}\mathbf{M}^{-1}\mathbf{W}_i\boldsymbol{\Delta}_i + \sum_{k\neq i} \mathbf{W}_i^{\mathrm{T}}\mathbf{M}^{-1}\mathbf{W}_k\boldsymbol{\Delta}_k + \mathbf{W}_i^{\mathrm{T}}\mathbf{M}^{-1}\mathbf{h}\Delta t + (1+\varepsilon_i)\gamma_i^A \tag{49}$$

for which the sum $\sum_{k\neq i}$ consists of only one element for curve squealing, we employ the abbreviations

$$\boldsymbol{\xi}_i \coloneqq \boldsymbol{\gamma}_i^E + \varepsilon_i \boldsymbol{\gamma}_i^A, \quad \mathbf{G}_{ij} \coloneqq \mathbf{W}_i^{\mathrm{T}} \mathbf{M}^{-1} \mathbf{W}_j, \quad \mathbf{c}_i \coloneqq \mathbf{W}_i^{\mathrm{T}} \mathbf{M}^{-1} \mathbf{h} \Delta t + (1+\varepsilon_i)\boldsymbol{\gamma}_i^A \tag{50}$$

to display it together with the normal cone inclusions of Eq. (47) as

$$\boldsymbol{\xi}_i = \mathbf{G}_{ii}\boldsymbol{\Delta}_i + \sum_{k\neq i} \mathbf{G}_{ik}\boldsymbol{\Delta}_k + \mathbf{c}_i, \quad \boldsymbol{\xi}_i \in \mathscr{N}_{\mathscr{A}_i}(-\boldsymbol{\Delta}_i). \tag{51}$$

After elimination of $\boldsymbol{\xi}_i$, one obtains an implicit inclusion for the unknown impulsive forces $\boldsymbol{\Delta}_i$,

$$\mathbf{G}_{ii}\boldsymbol{\Delta}_i + \sum_{k\neq i} \mathbf{G}_{ik}\boldsymbol{\Delta}_k + \mathbf{c}_i \in \mathscr{N}_{\mathscr{A}_i}(-\boldsymbol{\Delta}_i), \tag{52}$$

which can then be re-substituted into Eq. (48) to finally determine the endpoint velocities $\mathbf{u}_E$ needed for step 5 of the integration algorithm.

While inclusions of type (52) are most powerful instruments for analytical investigations, they cannot directly be implemented in numerical schemes. However, there is a way to equivalently express the normal cone inclusions as (nonlinear) equations, provided by the proximal point approach. We do not mean here any kind of regularization, but indeed an equivalent representation of them. We denote by $\mathbf{x} = \mathrm{prox}_{\mathscr{C}}(\mathbf{z})$ the proximal point to $\mathbf{z} \in \mathbb{R}^m$ in the convex set $\mathscr{C} \subset \mathbb{R}^m$, i.e. the point $\mathbf{x} \in \mathbb{R}^m$ which minimizes for given $\mathbf{z}$ the Euclidean distance $d(\mathbf{x}) = \|\mathbf{z}-\mathbf{x}\|$ under the constraint $\mathbf{x} \in \mathscr{C}$. Note that $\mathrm{prox}_{\mathscr{C}}(\mathbf{z})$ is the identity map for the case $\mathbf{z} \in \mathscr{C}$. It can now generally be shown [30] that the line segment $\mathbf{z}-\mathbf{x}$ from $\mathbf{x} \in \mathscr{C}$ to $\mathbf{z}$ is always contained in the normal cone of $\mathscr{C}$ at $\mathbf{x}$ and vice versa, which yields the equivalence $\mathbf{x} = \mathrm{prox}_{\mathscr{C}}(\mathbf{z}) \Leftrightarrow (\mathbf{z}-\mathbf{x}) \in r\mathscr{N}_{\mathscr{C}}(\mathbf{x})$ for any $r>0$. Multiplication with the scalar $r>0$ does not alter this result, because cones are by definition invariant under this operation. By setting now $\mathbf{y} \coloneqq (\mathbf{z}-\mathbf{x})/r$ and eliminating $\mathbf{z}$ from the above equivalence, we obtain $\mathbf{y} \in \mathscr{N}_{\mathscr{C}}(\mathbf{x}) \Leftrightarrow \mathbf{x} = \mathrm{prox}_{\mathscr{C}}(r\mathbf{y}+\mathbf{x})$ which can be used to write (51) as

$$\boldsymbol{\xi}_i = \mathbf{G}_{ii}\boldsymbol{\Delta}_i + \sum_{k\neq i} \mathbf{G}_{ik}\boldsymbol{\Delta}_k + \mathbf{c}_i, \quad -\boldsymbol{\Delta}_i = \mathrm{prox}_{\mathscr{A}_i}(r_i\boldsymbol{\xi}_i - \boldsymbol{\Delta}_i). \tag{53}$$

Final elimination of $\boldsymbol{\xi}_i$ yields an implicit equation for the unknown impulsive forces $\boldsymbol{\Delta}_i$,

$$-\boldsymbol{\Delta}_i = \mathrm{prox}_{\mathscr{A}_i}\left[(r_i\mathbf{G}_{ii} - \mathbb{1}_i)\boldsymbol{\Delta}_i + r_i \sum_{k\neq i} \mathbf{G}_{ik}\boldsymbol{\Delta}_k + r_i\mathbf{c}_i\right], \tag{54}$$

which can be iteratively solved by fixed point methods. In particular, blockwise Gauss–Seidel iteration has proven to be the most successful one when contact problems with Coulomb friction are treated. For a proper choice of the relaxation parameters r_i one should consult [9]. We finally want to mention that the nonlinear map $\mathrm{prox}_{\mathscr{C}} : \mathbb{R}^m \to \mathscr{C} \subset \mathbb{R}^m$ is continuous, weakly contractive and idempotent, which as a nonlinear projector makes it well suited for numerical evaluation.

The results of the simulations for curve squealing have been obtained with the standard midpoint rule described above and evaluation of the contact laws according to Eq. (54). For the restitution coefficients, the values $\varepsilon_N = \varepsilon_T = 0$ have been chosen. The simulation results will exemplarily be shown for the leading inner wheel with the initial condition corresponding to the black circle in the upper left stability chart of Fig. 8. Hence, we consider the run of a wheel with a diameter of 800 mm, a friction coefficient of 0.3 and the associated data which follow from Table 2. Fig. 10 shows the results of these simulations after the motion of the wheel has reached a periodic state and the initial transients have decayed. Fig. 10(a) shows the response of the friction force $(\lambda_{T1}^2 + \lambda_{T2}^2)^{1/2}$ (dotted line) which in stiction phases reduces to values much smaller than the stiction threshold $\mu\lambda_N$ (solid line). Both the longitudinal and lateral relative velocities γ_{T1} and γ_{T2} vanish during these stiction phases as is seen in Fig. 10(b). The phase planes of the longitudinal and lateral contact displacements are depicted in Figs. 10(c), (d) and reveal a limit cycle behavior. Note that the contact displacements are shown on the horizontal axes, whereas the contact velocities, being their time derivatives, are shown on the vertical axes. The latter equal the differences $\gamma_{Ti} - \chi_{Ti}$ of the relative velocities γ_{Ti} and the stationary creep velocities χ_{Ti}. Stiction ($\gamma_{Ti} = 0$) occurs in the phase planes when the contact velocities reach the lines of stiction indicated in the figures. The phase plane for the longitudinal direction clearly shows a corner in the limit cycle at the transition from sliding to stiction, i.e. when the line of stiction is hit, which is

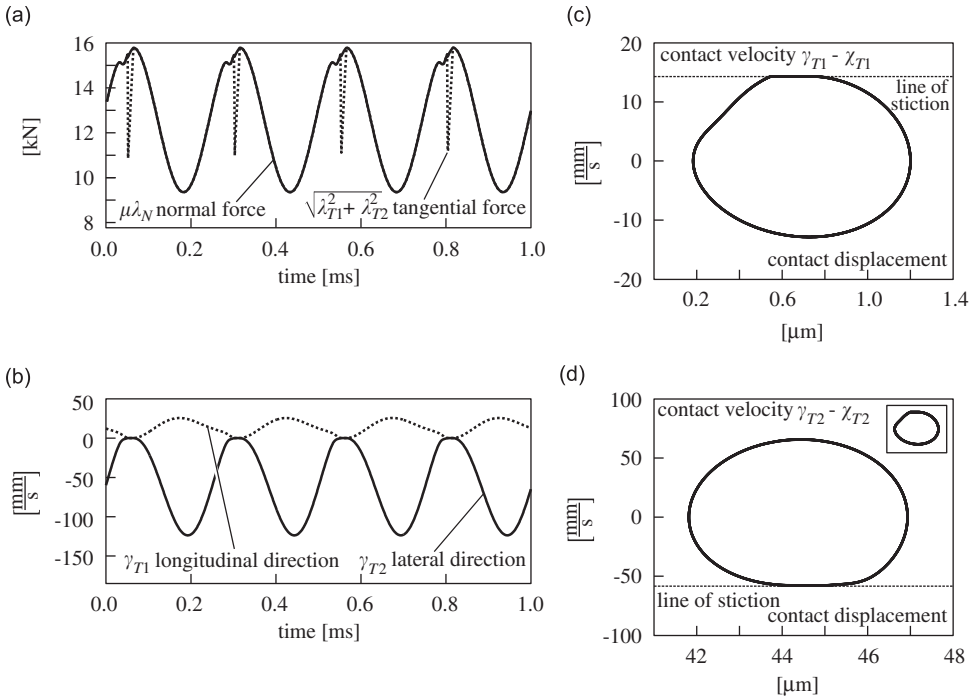

Fig. 10. Numerical simulation of the friction-induced self-excited oscillations at the leading inner wheel of the leading bogie: (a) time history of contact forces, (b) time history of tangential relative velocities, (c) limit cycle for longitudinal contact displacements and (d) limit cycle for transversal contact displacements.

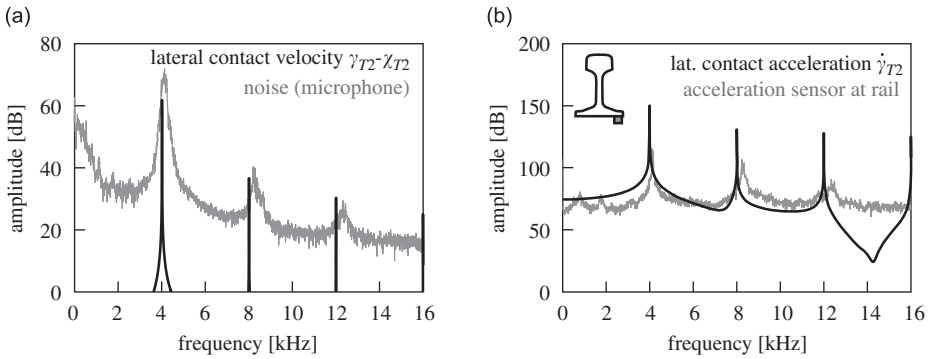

Fig. 11. Qualitative comparison of the frequency spectra at squeal obtained from numerical simulation and measurements: (a) velocity spectrum and (b) acceleration spectrum, both computed from the lateral contact motion.

typical for stick-slip oscillations. This non-smooth effect is also present in lateral direction but hardly visible. The motion in lateral direction is much larger than the one in longitudinal direction as can be seen from the comparative inset in the lower diagram. We emphasize that each calculation has been conducted with one and only one friction coefficient, being independent on velocity and time, which serves at the same time as static and dynamic friction coefficient. The friction-induced limit cycle shown in Fig. 10 has a frequency of about 3.99 kHz.

A qualitative comparison of simulations and measurements is depicted in Fig. 11. The diagrams in Fig. 11(a) show the frequency content of the measured squeal noise, i.e. the noise corresponding to the dashed line in Fig. 1, and the FFT of the lateral contact velocity. In Fig. 11(b), the measured frequency content of an acceleration sensor, being attached to the foot of the rail, is compared to the calculated lateral contact

acceleration. This comparison, which is of only qualitative nature, reveals that the relative intensity of the superharmonic resonances in the measurements and simulations agree quite well.

8. Conclusion

The proposed approach, which consists of a multibody simulation, a FE calculation and numerical analysis of the resulting system equations, enables us to completely describe the squeal phenomenon of railway vehicles. All phenomena related to squeal, which have occurred in the measurements or have been discussed with railway experts, can be explained by the results of the numerical calculations. Important parameters for the curve squeal phenomenon are the contact kinematical entities, i.e. the position of the contact point, the wheel–rail contact pairing, the lateral displacement, and the angle of attack. Of equal importance is the geometry of the wheel which determines its eigenforms and frequencies, and of course the friction coefficient. The particular form of the friction curve, which is normally regarded to be of prime importance, plays in fact only a minor role. At present, three modes of the free wheel with fixed center nodes can be identified to be essential for the squeal mechanism. These three modes have to occur at similar frequencies, one for which the wheel oscillates in lateral direction at its rim, and two radial modes which allow for a variation of the normal force.

Each calculation step presented in the paper opens the way to test arbitrary wheel designs and railway profiles on their vulnerability for squeal, in order to propose targeted changes in their design. From the theoretical point of view, a detailed bifurcation analysis of the system has still to be conducted. Furthermore, it still needs to be clarified how the choice of the eigenmodes in the system reduction influences the results, and whether the squeal phenomenon might finally be reduced to only two relevant modes.

References

[1] E. Cataldi-Spinola, Curve squealing mechanism of railway vehicles, Diss. ETH No. 17453, ETH Zurich, 2007.
[2] R. Stefanelli, Kurvenkreischen: Untersuchung der Rahmenbedingungen, die zu Kreischen führen, und akustische Modellierung der kreischenden Räder (Curve squealing: Investigation of the General Conditions which lead to Squeal, and Acoustic Modelling of the Squealing Wheels), Diss. ETH No. 16686, ETH Zurich, 2006.
[3] H. Stappenbeck, Das Kurvengeräusch der Strassenbahn (The curve noise of the tramway), *VDI Zeitschrift des Vereins Deutscher Ingenieure* 96 (6) (1954) 171–175.
[4] H. Berglund, Stockholm tackles the noise problem, *Railway Gazette International* (1972) 254–259.
[5] D.J. Thompson, Wheel–rail noise generation, part V: inclusion of wheel rotation, *Journal of Sound and Vibration* 161 (3) (1993) 467–482.
[6] J. Grajnert, O. Krettek, Zur Phänomenologie und Ersatzmodellbildung von Luftfedern (On the phenomenology and process of modelling of air springs), ZEV + DET *Glasers Annalen* 115 (7/8) (1991) 218–223.
[7] O. Polach, Rad-Schiene-Modelle in der simulation der Fahrzeug- und Antriebsdynamik (Wheel–rail models in the simulation of vehicle and power transmission dynamics), *Elektrische Bahnen* 99 (5) (2001) 219–230.
[8] Ch. Glocker, Set-valued force laws, *Lecture Notes in Applied Mechanics*, Vol. 1, Springer, Berlin, Heidelberg, 2001.
[9] Ch. Studer, Augmented time-stepping integration of non-smooth dynamical systems, Diss. ETH No. 17597, ETH Zurich, 2008.
[10] M. Rudd, Wheel/rail noise—part II: wheel squeal, *Journal of Sound and Vibration* 46 (3) (1976) 381–394.
[11] P.J. Remington, Wheel/rail squeal and impact noise: What do we know? What don't we know? Where do we go from here?, *Journal of Sound and Vibration* 116 (1987) 339–353.
[12] F.J. Periard, Wheel–rail noise generation: Curve squealing by trams, PhD Thesis, TU Delft, 1998.
[13] E. Schneider, K. Popp, H. Irretier, Noise generation in railway wheel due to rail–wheel contact forces, *Journal of Sound and Vibration* 120 (2) (1988) 227–244.
[14] A.A. Andronov, A.A. Vitt, S.E. Khaikin, *Theory of Oscillators*, Pergamon Press, Oxford, 1966 (translated from Russian).
[15] J.J. Stoker, *Nonlinear Vibrations in Mechanical and Electrical Systems*, Interscience Publishers, New York, 1950.
[16] A.D. Monk-Steel, D.J. Thompson, F.G. de Beer, M.H.A. Janssens, An investigation into the influence of longitudinal creepage on railway squeal due to lateral creepage, *Journal of Sound and Vibration* 293 (2006) 766–776.
[17] R.T. Spurr, Frictional oscillations, *Nature* 189 (475) (1961) 50–51.
[18] R.A. Ibrahim, Friction-induced vibration, chatter, squeal, and chaos; part II: dynamics and modeling, *ASME Applied Mechanics Reviews* 47 (7) (1994) 227–253.
[19] R.I. Leine, B. Brogliato, H. Nijmeijer, Periodic motion and bifurcations induced by the Painlevaé paradox, *European Journal of Mechanics—A/Solids* 21 (5) (2002) 869–896.

[20] J.A.C. Martins, S. Barbarin, M. Raous, A. Pinto da Costa, Dynamic stability of finite dimensional linearly elastic systems with unilateral contact and coulomb friction, *Computer Methods in Applied Mechanics and Engineering* 177 (1999) 289–328.
[21] Ch. Glocker, *Dynamik von Starrkörpersystemen mit Reibung und Stößen* (*Dynamics of Rigid Body Systems with Friction and Impacts*), VDI-Fortschrittberichte Mechanik/Bruchmechanik Reihe 18 Nr. 182, VDI-Verlag, Düsseldorf, 1995.
[22] F. Pfeiffer, Ch. Glocker, *Multibody Dynamics with Unilateral Contacts*, Wiley, New York, 1996.
[23] S.H. Strogatz, *Nonlinear Dynamics and Chaos with Application to Physics, Biology, Chemistry and Engineering*, Addison-Wesley, Reading, MA, 1994.
[24] J.J. Moreau, Bounded variation in time, in: J.J. Moreau, P.D. Panagiotopoulos, G. Strang (Eds.), *Topics in Nonsmooth Mechanics*, Birkhäuser, Basel, 1988, pp. 1–74.
[25] Ch. Glocker, An introduction to impacts, in: J. Haslinger, G. Stavroulakis (Eds.), *Nonsmooth Mechanics of Solids, CISM Courses and Lectures*, Vol. 485, Springer, Wien, 2006, pp. 45–102.
[26] J.J. Moreau, Unilateral contact and dry friction in finite freedom dynamics, in: J.J. Moreau, P.D. Panagiotopoulos (Eds.), *Non-Smooth Mechanics and Applications, CISM Courses and Lectures*, Vol. 302, Springer, Wien, 1988, pp. 1–82.
[27] J.J. Moreau, Numerical aspects of the sweeping process, *Computer Methods in Applied Mechanics and Engineering* 177 (1999) 329–349.
[28] V. Acary, B. Brogliato, Numerical methods for nonsmooth dynamical systems, *Lecture Notes in Applied and Computational Mechanics*, Vol. 35, Springer, Berlin, Heidelberg, 2008.
[29] R.I. Leine, N. van de Wouw, Stability and convergence of mechanical systems with unilateral constraints, *Lecture Notes in Applied and Computational Mechanics*, Vol. 36, Springer, Berlin, Heidelberg, 2008.
[30] Ch. Glocker, Simulation von harten Kontakten mit Reibung: Eine iterative Projektionsmethode (Simulation of hard contacts with friction: an iterative projection method), *Schwingungen in Antrieben 2006 Tagung*, VDI-Berichte Nr. 1968, VDI-Verlag, Düsseldorf, 2006, pp. 19–44.